

**UNIVERSITY OF TURKISH AERONAUTICAL ASSOCIATION
INSTITUTE OF SCIENCE AND TECHNOLOGY**

**ROLE OF INTERPHASE AND CHARACTERIZATION OF POLYMER
NANOCOMPOSITES USING FTIR, TGA AND SEM**

MASTER THESIS

Sadeq M. Hassen Alewei AL-KHIDHRI

**Mechanical and Aeronautical Engineering Department
Master Thesis Program**

JUNE, 2017

**UNIVERSITY OF TURKISH AERONAUTICAL ASSOCIATION
INSTITUTE OF SCIENCE AND TECHNOLOGY**

**ROLE OF INTERPHASE AND CHARACTERIZATION OF POLYMER
NANOCOMPOSITES USING FTIR, TGA AND SEM**

MASTER THESIS

Sadeq M. Hassen Alewei AL-KHIDHRI

ID: 1406080002

**Mechanical and Aeronautical Engineering Department
Master Thesis Program**

Supervisor: Assoc. Prof. Dr. Murat Demiral

JUNE, 2017

بِسْمِ اللّٰهِ الرَّحْمٰنِ الرَّحِیْمِ

الْأَرْضِ مِثْلُ نُوْرِهِ ۗ اللّٰهُ نُورٌ السَّمٰوٰتِ وَ
كَمِشْكَاتٍ فِيْهَا مِصْبَاحٌ ۗ الْمِصْبَاحُ فِي زُجَاجَةٍ
الزُّجَاجَةُ كَأَنَّهَا كَوْكَبٌ دُرِّيٌّ يُوقَدُ مِنْ شَجَرَةٍ
مُّبَارَكَةٍ زَيْتُوْنَةٍ لَّا شَرْقِيَّةٍ وَ لَّا غَرْبِيَّةٍ يَكَادُ
زَيْتُهَا يُضِيئُ ۖ وَ لَوْ لَمْ تَمْسَسْهُ نَارٌ نُّوْرٍ عَلٰى
نُّوْرِ يَهْدِي اللّٰهُ لِنُوْرِهِ ۗ مَنْ يَشَآءُ وَيَضْرِبُ اللّٰهُ
الْأَمْثَالَ لِلنَّاسِ وَ اللّٰهُ بِكُلِّ شَيْءٍ عَلِیْمٌ

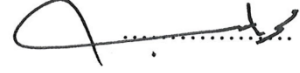
صدق الله العظيم (سورة النور ٣٥)

Türk Hava Kurumu Üniversitesi Fen Bilimleri Enstitüsü'nün 1406080002 numaralı Yüksek Lisans öğrencisi “Sadeq AL-KHIDHRI” ilgili yönetmeliklerin belirlediği gerekli tüm şartları yerine getirdikten sonra hazırladığı ‘ROLE OF INTERPHASE AND CHARACTERIZATION OF POLYMER NANNOCOMPOSITE USING FTIR, TGA AND SEM’ başlıklı tezini aşağıda imzaları bulunan jüri önünde başarı ile sunmuştur.

Tez Danışmanı : Doç. Dr. Murat Demiral
Çankaya Üniversitesi



Jüri Üyeleri : Yrd. Doç. Dr. Mohamed Salem Elmnefi
Türk hava kurumu üniversitesi



: Yrd. Doç. Dr. Muharrem Kunduraci
Türk hava kurumu üniversitesi



: Doç. Dr. Murat Demiral
Çankaya Üniversitesi



Tez Savunma Tarihi: 29.06.2017

STATEMENT OF NON-PLAGIARISM PAGE

I hereby declare that all information in this document has been obtained and presented in accordance with academic rules and ethical conduct. I also declare that, as required by these rules and conduct, I have fully cited and referenced all material and results that are not original to this work.



29.06.2017

Sadeq AL-KHIDHRI

ACKNOWLEDGEMENTS

Before anything, thanks to God Almighty for the blessing and for giving me the health and strength to complete my thesis successfully. I hope that God will always help and bless me in the future.

I would like to express my grateful and my sincere appreciation to my kind supervisor Assoc. Prof. Dr. Murat Demiral and Prof. Dr. Adel K. Mahmoud for their continuous support and valuable guidance in the preparation of this study. Without their continuous support and encouragement, this thesis would not have been the same as presented here.

I place on record my sincere gratitude to my Father and my Wife who support and help me in every step of my life.

I also extend my thanks and appreciation to the University of Technology – Material Engineering Department, Baghdad-Iraq, especially to Prof. Dr. Adel K. Mahmoud for the help and assistance in conducting the experimental works.

I also place on record my sincere gratitude to the staff of the University of Turkish Aeronautical Association, Institute of Science and Technology and Mechanical Engineering Department.

JUNE, 2017

Sadeq AL-KHIDHRI

TABLE OF CONTENTS

ACKNOWLEDGEMENTS	iv
TABLE OF CONTENTS	v
LIST OF FIGURES	vii
LIST OF TABLES	x
LIST OF SYMBOLS	xi
LIST OF ABBRIVIATION	xiii
ABSTRACT	xvi
ÖZET	xviii
CHAPTER ONE	1
Introduction	1
1.1 Polymer Nanocomposite Materials	1
1.2 The Matrix- filler interphase	2
1.3 The Aims of the Present Work	3
1.4 Thesis Outline	4
CHAPTER TWO	5
Nanocomposite Testing Techniques and Literature Review	5
2.1 Introduction	5
2.2 Nanoparticle Dispersion	5
2.3 Nanocomposite Testing Techniques	5
2.3.1 Tensile Testing	5
2.3.2 Thermal Gravimetric Analysis (TGA)	7
2.3.3 Scanning Electron Microscope (SEM)	7
2.3.4 Fourier Transform Infrared Spectroscopy (FTIR)	8
2.4 Literature review	9
CHAPTER THREE	16
Experimental works	16
3.1 Introduction	16
3.2 System initial mixture	16
3.3 Tests and inspection	20
3.3.1 Tensile test	20

3.3.2 Thermal Gravimetric Analysis TGA	28
3.3.3 Scanning electron microscopy SEM	29
3.3.4 Fourier Transform Infrared Spectroscopy FTIR	30
CHAPTER FOUR	32
Results and discussion	32
4.1 Introduction	32
4.2 Tensile test results	32
4.3 Scanning electron microscopy (SEM)	39
4.4 Fourier transform infrared spectroscopy (FTIR)	49
4.5 Thermal Gravimetric Analysis (TGA)	56
4.6 Interphase Characterization	58
CHAPTER FIVE	65
Conclusions and Recommendations	65
5.1 Conclusions	65
5.2 Suggestions for future works	67
REFERENCES	68

LIST OF FIGURES

Figure 1-1. Schematic of interphase area between a filler and the polymer matrix [13].	2
Figure 1-2. Metal-polymer nanocomposite and metal oxide clusters surface adsorption attributes when (a) a strongly-binding polymer (b) a weakly-binding polymer adheres [2].	4
Figure 2-1. Standard tensile specimen with circular cross section [25].	6
Figure 2-2. Schematic representation of tensile test machine.	7
Figure 3-1. Specifications of the PS (pure/reference) Matrix.	18
Figure 3-2. The specifications of the PMMA (pure/reference) Matrix.	18
Figure 3-3. Shows the specifications of the Fe ₂ O ₃ nanoparticles.	19
Figure 3-4. Shows the specifications of the Al ₂ O ₃ nanoparticles.	19
Figure 3-5. Tensile test sample (a) Top view (b) Side view (c) 3D view.	22
Figure 3-6. The designed mold.	23
Figure 3-7. The air bubbles in manufactured sampels.	23
Figure 3-8. Cross section of mold, sample and punch assembly	24
Figure 3-9. Mold, sample and punch assembly.	25
Figure 3-10. WDW-200e tensile test machine.	26
Figure 3-11. Fourier Transform Infrared Spectroscopy (Perkin Elmer Spectrum 100).	31
Figure 4-1. the stress-strain curve for Ash, et al. [30].	35
Figure 4-2. Load-extension curves for PMMA group.	35
Figure 4-3. Load-extension curves for PS group	36
Figure 4-4. Engineering stress strain curves for PMMA group	36
Figure 4-5. Engineering stress strain curves for PS group	37
Figure 4-6. True stress-strain curves for PMMA group.	37
Figure 4-7. True stress-strain curves for PS group.	38
Figure 4-8. SEM image with low magnification view of particle dispersion for s of PMMA – Fe304.	40

Figure 4-9. SEM image with close-up view of a small flocculant for s of PMMA – Fe ₃ O ₄	41
Figure 4-10. SEM image with low magnification view of particle dispersion for s of PS – Fe ₃ O ₄	42
Figure 4-11. SEM image with close-up view of a small flocculant for s of PS – Fe ₃ O ₄	43
Figure 4-12. PMMA – Al ₂ O ₃ SEM image with low magnification view of a large flocculant.....	44
Figure 4-13. PMMA – Al ₂ O ₃ SEM image with close-up view of the particles within the flocculant.....	44
Figure 4-14. PS – Al ₂ O ₃ SEM images with low magnification view of particle dispersion	45
Figure 4-15. PS – Al ₂ O ₃ SEM images with close-up view of a small flocculant....	45
Figure 4-16. SEM image with measuring tools applied on the PMMA – Al ₂ O ₃ tensile test specimen at fracture	47
Figure 4-17. Image with measuring tools applied on the PMMA – Fe ₃ O ₄ tensile test specimen at fracture	48
Figure 4-18. Image with measuring tools applied on the PS – Al ₂ O ₃ tensile test specimen at fracture	48
Figure 4-19. SEM image with measuring tools applied on the PS – Fe ₃ O ₄ tensile test specimen at fracture.....	49
Figure 4-20. FTIR spectra for PMMA – Al ₂ O ₃ , PMMA – Fe ₃ O ₄ , and PMMA – chlorobenzene systems showing the peak indicators for the 2843.8 band indicating broken O— CH ₃	52
Figure 4-21. FTIR spectra for PMMA – Fe ₃ O ₄ , PMMA – Al ₂ O ₃ , a PMMA – chlorobenzene systems showing the peak indicators for the 1731 band indicating C == O is no longer isolated in some PMMA segments.....	52
Figure 4-22. FTIR spectra for PMMA – Al ₂ O ₃ , PMMA – Fe ₃ O ₄ , and PMMA – chlorobenzene systems showing 1683 cm – 1 band indicating the absorbance of the carboxylic base (COO) groups.....	53

Figure 4-23. FTIR spectra for PMMA – Al₂O₃, PMMA – Fe₃O₄ , and PMMA – chlorobenzene systems showing the 1166.7 and 1143 cm – 1 bands. Notice the shift in peak ratio between the chlorobenzene and the nanocomposite spectra. 54

Figure 4-24. PMMA based sysgtem TGA results 57

Figure 4-25. The PS-based systems TGA results..... 58

Figure 4-26. (a) The effective average polymer layer adsorbed on the nanoparticle, (b) The actual number of free repeating units that exist in a polymer loop 59



LIST OF TABLES

Table 3-1. Constituents used to make polymer nanocomposite systems.	17
Table 4-1. Tensile test mechanical properties for PMMA group	38
Table 4-2. Tensile test properties for PS group.....	38
Table 4-3. The change in the Ultimate strength and strain.....	39
Table 4-4. The computed particles size in nm as measured from SEM images.....	49
Table 4-5. Infrared absorption bands of PMMA segment adsorption on Al ₂ O ₃ surfaces.....	52
Table 4-6. The number of anchors per chain computed from FTIR results for PMMA – Al₂O₃ and PMMA – Fe₃O₄	56
Table 4-7. The computed interphase density results using the SEM and TGA data .	63

LIST OF SYMBOLS

Symbol	Description	Units
$\%e$	the percentage elongation	%
\overline{M}_W	averaged molecular weight	
A_o	the initial cross section area of the sample	mm^2
D_{av}	average diameter of clusters	nm
$D_{clusrter}$	average diameter of clusters	nm
D_o	sample Initial diameter	mm
L_{eff}	The thickness of the polymer layer	mm
L_o	sample Initial length	mm
M_{sample}	mass of the TGA sample	g
M_w	molecular weight	
$M_{w-molecule}$	molecular weight of one metal oxide molecule in cluster	g/mol e
N_A	the number of chains per mole (Avogadro's Number)	$\frac{chains}{mole}$
$N_{cluster}$	the number of clusters in the sample	
$N_{molecule/cluster}$	number of molecules per cluster	
$N_{molecules}$	total number of molecules in sample	
$N_{segments}$	the average segments in chain	
$V_{cluster}$	metal oxide cluster volume	
$V_{polymer}$	volume of the polymer layer bound to the surface	
V_{total}	The Total volume of the capped particle	
$d_{molecule}$	diameter of a molecule	nm
n_{eff}	average number of repeating units	

n_{loop}	the minimum number of segments present in a loop	
$w_{cluster}$	mass fraction of polymer after decomposition of the polymer as obtained from TGA result	%
$w_{polymer}$	the weight fraction of the polymer	%
$\rho_{molecule}$	density of molecule	$\frac{g}{nm^3}$
σ_h	steric hindrance factor	
σ_e	the engineering stress	MPa
ΔL	the change in length	mm
A	instantaneous area	mm^2
A_c	the number of anchoring points per chain	
E	modulus of elasticity	GPa
F	the applied force	N
L	instantaneous length	mm
e	engineering strain	
l	C-C bond length	Å
ε	volume fraction of the molecules in the cluster	
θ	rotation angle for C-C bonds	degree
ρ	density of a thin polymer film	$\frac{g}{nm^3}$
σ	true stress	MPa
ϵ	true strain	

LIST OF ABBREVIATIONS

Abbreviation	Description
CuO	unmodified cupric oxide
DSC	The differential scanning calorimetry
EDS	Energy-dispersive X-ray spectroscopy
FTIR	The Fourier transform infrared spectroscopy
HRP	the horseradish peroxidase
MgO	magnesium oxide
MPS	methacryloxypropyl-trimethoxysilane
NBR	Acrylonitrile Butadiene Rubber
NMR	nuclear magnetic resonance spectroscopy
NPs	anatase TiO_2 nanoparticles
PANI	Polyaniline
PMMA	poly methyl methacrylate
PP	polypropylene
PS	polystyrene
PSf	polysulfide
SEC	size exclusion chromatography
SEM	Scanning Electron Microscope

TEM	transmission electron microscope
T _g	Glass change temperatures
TGA	Thermal gravimetric analysis
UV-Vis.	Ultraviolet–visible spectroscopy
VTES	grafting vinyl triethoxysilane
<i>CaCo₃</i>	calcium carbonate
<i>MAS²⁹Si</i>	magic-angle spinning
SPS	sulfonated polystyrene
SSM	mixing solid-state modification

ABSTRACT

ROLE OF INTERPHASE AND CHARACTERIZATION OF POLYMER NANOCOMPOSITES USING FTIR, TGA AND SEM

AL-KHIDHRI, Sadeq M. Hassen

Master, Mechanical and Aeronautical Engineering Department

Thesis Supervisors: Assoc. Prof. Dr. Murat Demiral

JUNE, 2017, 72 pages

This work aims to build four polymer nanocomposite systems and test them to compare their mechanical properties with their pure polymer matrix. Aluminum oxide (Al_2O_3) and magnetite (Fe_3O_4) nanoparticles were inserted into poly(methyl methacrylate) (PMMA) and polystyrene (PS) matrices. Tensile tests were applied for all systems and showed that these four polymer nanocomposite systems have bad mechanical properties compared to their particular pure polymer systems.

An investigation was conducted to consider the interphase between the polymer matrix and the nanoparticles. This investigation was applied using two approaches to explain the results of the tensile tests. The first strategy implemented data taken from applying the thermal gravimetric analysis (TGA) and scanning electron microscopy (SEM) to estimate the structure and density of the interphase for the four nanocomposite systems. The other strategy examined the bonding between the nanoparticle surfaces and the polymer utilizing Fourier Transform Infrared Spectroscopy (FTIR) to estimate the density of the interphase for two PMMA-based

nanocomposite systems. The results showed that Al_2O_3 nanoparticles have more reactivity with the polymer matrix than Fe_3O_4 nanoparticles; however, both had weak interaction with the polymer matrix. This weak interaction reduced the interphase density, which resulted in worse mechanical properties of the polymer nanocomposite material reinforcement by Fe_3O_4 nanoparticles.



ÖZET

İTERFAZIN ROLÜ VE FOURIER DÖNÜŞÜMLÜ KIZILÖTESİ SPEKTROSKOPİSİ, TERMOGRAVİMETRİK ANALİZİ, TARAMALI ELEKTRON ELEKTROSKOPU KULLANARAK POLİMER NANOKOMPOZİTİN KARAKTERİZASYONU

AL-KHIDHRI, Sadeq M. Hassen

Yüksek Lisans, Makine Mühendisliği anabilim dalı

Tez Danışmanı: Doç. Dr. Murat Demiral

HAZİRAN, 2017, 72 sayfa

Bu çalışma dört polimer nanokompozit sistemlerin kurulmasını ve saf polimer matriksleri ile mekanik özelliklerini karşılaştırma amaçlı test edilmelerini amaçlamaktadır. Alüminyum Al_2O_3 ve manyetit Fe_3O_4 nanopartiküller poli (metil metakrilat) (PMMA) ve polistiren(PS) matrislerine eklenmiştir. Çekme tüm sistemler için uygulanmış ve dört polimer nanokompozit sistemlerin, özel saf polimer sistemlerine oranla kötü mekanik özellikleri olduğunu göstermiştir.

Polimer matriks ve nanopartiküller arasındaki interfazı incelemek için bir araştırma düzenlenmiştir. Bu araştırma, iki yaklaşımın kullanılması ile çekme deneyinin sonuçlarını açıklamak için yapılmıştır. İlk strateji, dört nanokompozit sistemlerin interfaz yoğunluğu ve yapısı hakkında değerlendirme yapmak için yapılan termogravimetrik analiz (TGA) ve taramalı elektron elektroskop (SEM) yöntemlerinin uygulanmasıyla alınan verileri uygulamıştır. Diğer strateji ise; iki PMMA–temelli nanokompozit sistemlerin interfaz yoğunluğunu değerlendirmek için yapılan Fourier Dönüşümlü Kızılötesi Spektroskopisi (FTIR) yönteminin kullanılması ile nanopartikül yüzeyler ve polimer arasındaki bağlanmayı test etmiştir. Sonuçlar; Al_2O_3 nanopartiküllerin Fe_3O_4 nanopartiküllere oranla daha tepkiselliğe girdiğini ortaya çıkarmıştır, şunu da belirtmek gerekir ki her ikisinin de polimer matrisle zayıf etkileşimi vardır. Bu zayıf etkileşim; Fe_3O_4 nanopartiküller ile yapılan polimer nanokompozit malzeme takviyesinin, daha kötü mekanik özelliklere sahip olmasına neden olan interfaz yoğunluğunu azaltmıştır.

CHAPTER ONE

INTRODUCTION

1.1 Polymer Nanocomposite Materials

Polymer nanocomposites have drawn important attention from both industry and academia as they typically exhibit significant developments in material properties at extremely fine grades with small nano-filler loadings in comparison to pure polymers or conventional composites. Polymer nanocomposites are a specialized type of polymer composite, a type of reinforced polymer creating a two-phase material along with the reinforcing phase acquiring a minimum of one dimension at the $10^{-9} m$ (*nm*) scale. It produces a new type of material using nanoscale dispersion, usually 1 to 100 *nm*, of the filler phase inside a given matrix [1].

A polymer composite is a mix of a polymer matrix and a strong reinforcing phase or filler. Polymer composites have attractive properties that are not only available in matrix or filler elements [2]. A polymer nanocomposite is a polymer matrix with a reinforcing phase including particles along with a particular dimension inside the nano-sized regime. In earlier decades, comprehensive studies provided concentrates on polymer nanocomposites hoping to take advantage of the initial properties of materials at the nano-sized regime [3]. The nanocomposites exhibit considerably enhanced mechanical properties over their micro-sized counterparts [4]. The nano-particles contain higher high surface-to-volume ratios and provide high energy surfaces due to their small size. A predicted result of embedding nanoparticles into a polymer matrix includes improved bonding involving the polymer matrix and filler caused by the high interfacial energy of the nanoparticles [5]. The polymer composite principle anticipates that enhanced bonding concerning the polymer and matrix can lead to better mechanical properties [5] [6].

Mechanical tests associated with nanocomposites have revealed compound results. Several experimental data have proved that minimized particle size increases mechanical properties, mainly the elastic modulus [7] [8] [9]. Additional studies have indicated that the elastic modulus decreases with reduced dimensionality. Certainly, no clear conclusions are generally made relating to developments of the mechanical properties of polymer nanocomposites [7] [8] [10].

Although research has concentrated on several matrix-filler systems, a typical characteristic of all polymer composites is the presence of a phase border relating to the matrix and filler along with the creation of an interphase layer connecting them. The properties of the interphase may differ considerably through the bulk and affect the mechanical properties for the composite. To clarify the effect on properties, many theories have been utilized for the analysis of interphase [10] [11].

1.2 Matrix-Filler Interphase

Regardless of the massive number of polymer composite systems, a typical thread concerning most systems is the presence of a phase border between the matrix and filler and also the creation of an interphase layer between them [12]. Figure 1-1 shows the interphase area between the matrix and the filler. It can be seen from Figure 1-1 that the interphase layer extends even further than the adsorption layer with the matrix chains bound to the filler surface. The composition of the interphase differs in comparison to either the filler or matrix phases, and it also varies based on the distance from the bound surface [13].

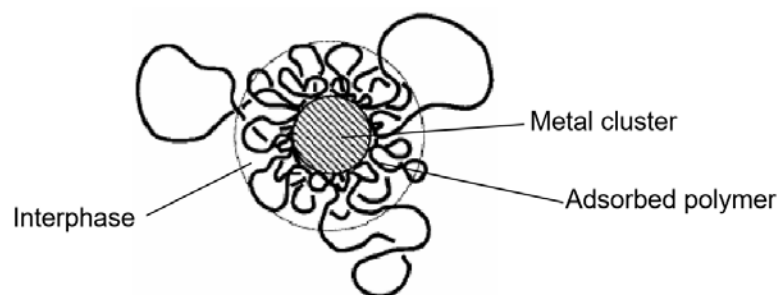


Figure 1-1 Schematic of interphase area between a filler and the polymer matrix [13]

Due to the variations in structure, interphase attributes may vary considerably from the bulk polymer [14]. The interphase is an essential factor affecting the mechanical properties of the composite because its distinctive properties influence the load transfer between the matrix and filler [15]. However, due to the large surface area of the nanoparticles, the interphase can easily dominate the properties of nanocomposites. [12]. An interphase 1 nm thick on the microparticles in a composite represents as little as 0.3% of the total composite volume. As displayed in Figure 1-1, the interphase contains an attributes structure consisting of flexible polymer chains, commonly in sequences of adsorbed segments (trains), loops, and tails. Interphase thickness is a variable value due to the fact that the interphase does not have a defined border along with the bulk polymer. The effective value of the thickness varies according to the chain flexibility and energy of adsorption which depends on the polymer surface energies and the solid. As a result of conformational restrictions introduced by surface and statistical conformations of the polymer's coils in solutions, relatively few segments can be bound to the surface [16]. If every area of the surface has adsorption capability, if the polymer chain is normally flexible, and if the segments are readily adsorbed, the loops will be small and the macromolecule may create a flat layer near the surface, as illustrated in Figure 1-2a. In case the chain segment interaction along with the surface becomes weak, or in case the chain is rigid, the loops and tails can extend farther inside the matrix and create an area with reduced density, as displayed in Figure 1-2b.

The concept of an interphase has become widely accepted although the effects of the interphase on the properties of the polymer composite still have not been quantitatively identified [17]. Several studies have revealed the interphase as a significant parameter on the mechanical properties of composites [18].

1.3 Aims of the Present Work

This work aims to build four types of polymer nanocomposite systems and experimentally define their mechanical properties as well as the effect of the interphase on their behavior. These four systems are constructed based on two main polymer matrices, polystyrene (PS) and poly(methyl methacrylate) (PMMA).

Aluminum (Al_2O_3) nanoparticles are dispersed into these two matrices constructing the first two systems, whereas magnetite Fe_3O_4 nanoparticles are dispersed into the two matrices constructing the other two systems. Four experiments are conducted to examine the nanocomposite systems. The tensile test samples are prepared to determine the mechanical properties. A scanning electron microscope (SEM) is utilized to identify the particle sizes and their distributions. Fourier transform infrared spectroscopy (FTIR) and thermal gravimetric analysis (TGA) are utilized to examine the interphase bonding, density and thickness.

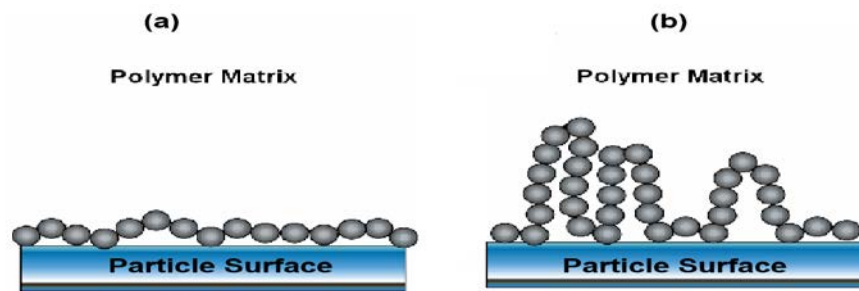


Figure 1-2 metal-polymer nanocomposite and metal oxide clusters surface adsorption attributes when (a) a strongly-binding polymer and (b) a weakly binding polymer adheres [2]

1.4 Thesis Outline

The current thesis is divided into five chapters:

Chapter One includes the general introduction about nanocomposite materials and the aims of the present work followed by a description of a brief survey of scientific studies in Chapter Two. The third chapter explains the sample preparation and the principles of the applied experiments as well as the testing instruments that are to be utilized. Chapter Four presents the results and an analysis of the data, in addition to an explanation of the results. Finally, Chapter Five covers the conclusions and makes suggestions for future work.

CHAPTER TWO

NANOCOMPOSITE TESTING TECHNIQUES AND LITERATURE REVIEW

2.1 Introduction

This chapter describes the theoretical background and reviews a number of articles from the published literature which are typically associated with the scope of this work.

2.2 Nanoparticle Dispersion

The dispersion of the nanoparticles through the polymer matrix is a significant factor affecting the attributes of a nanocomposite [19]. The dispersion of an inorganic nanoparticle filler in a thermoplastic is not simply obtained due to the nanoparticles exhibiting a hard tendency to agglomerate to lower their surface energy. Rong, et al., [18] implemented grafting polymers to encircle nanoparticles and generate improved dispersion. Several studies implemented adsorbed polymers to make the nanoparticle dispersions sterically stable and to restrict the creation of flocculants and aggregates [20, 21]. Various studies use several strategies of in-situ polymerization to attain better particle dispersion [22, 23]. However, the research previously mentioned implemented numerous sample preparation approaches, and no approach proved to be considerably better than any other approach [24].

2.3 Nanocomposite Testing Techniques

2.3.1 Tensile Testing

One of the most standard mechanical stress-strain tests is carried out in tension. The tension test may be conducted to assess various mechanical properties of

materials that will be fundamental in a design. A specimen is deformed, generally to fracture, including a gradually rising tensile load that is applied uniaxially across the long axis associated with a specimen [25]. A standard tensile specimen is shown in Figure 2-1.

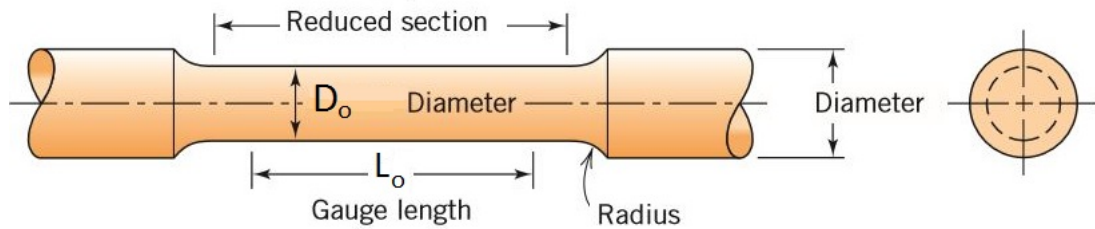


Figure 2-1 standard tensile specimen with circular cross section [25]

Generally, cross sections are circular although rectangular specimens can also be used. In this research, the circular configuration of the tensile specimens is used. This “dog bone” specimen setup was selected so that, during the course of testing, deformation can be limited to the narrow center region (which contains a uniform cross section along the length of the specimen), and also to lower the probability of fracture in the specimen ends. The tensile testing machine was configured to elongate the specimen at a constant rate of elongation, and regularly and simultaneously estimate the instantaneous applied load (with a load cell) and the resulting elongations (using an extensometer). A stress-strain test normally takes a few minutes to execute and is destructive; that is, the test specimen is actually permanently deformed and typically fractured [25]. The specimen can be fitted from its ends on the holding grips of the tensile testing machine, as shown in Figure 2-2. The results of this test can be recorded (usually on a computer) as load or force versus elongation. These load-extension data are dependent upon the specimen size. From the load-extension data, the material properties, such as the elastic modulus, yield stress, yield strain, ultimate stress, and ultimate strain, can be computed. The American Society for Testing and Materials (ASTM) affords the following appropriate standard test methods:

- D638 – Tensile Properties of Plastics
- D3039 – Tensile Properties of Polymer Matrix Composite Materials

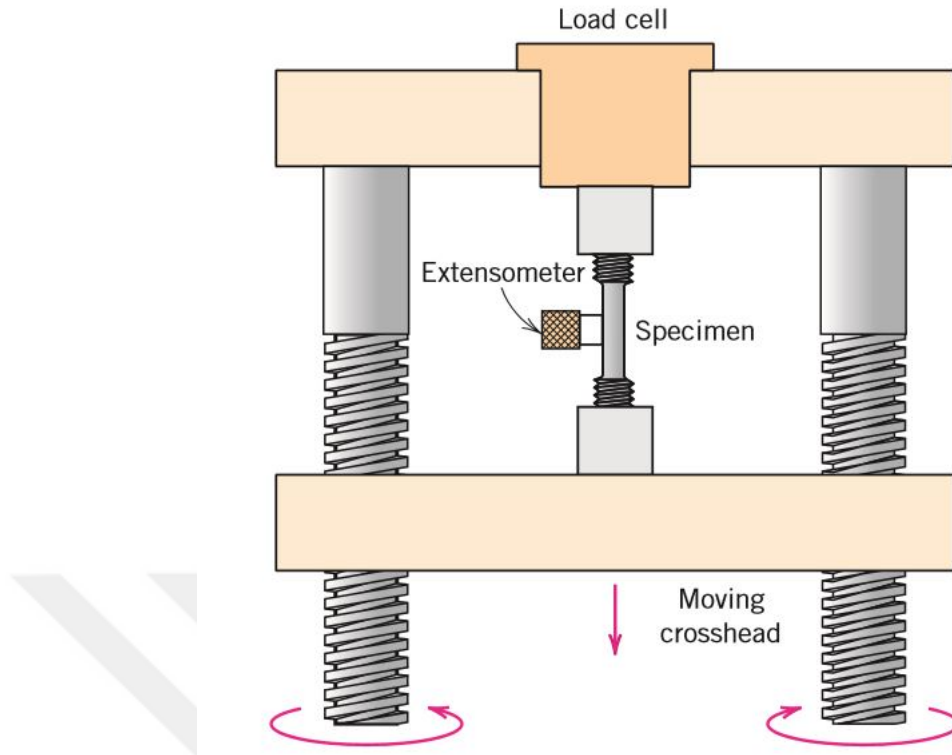


Figure 2-2 Schematic representation of the tensile test machine

2.3.2 Thermal Gravimetric Analysis (TGA)

Thermal gravimetric analysis (TGA) is utilized to obtain the modification in polymer decomposition temperatures involving the several samples and it identifies the thickness of the polymer layer surrounding the nanoparticles. TGA regularly measures the sample weight as a function of both temperature and time. The sample is placed onto a tray in a microbalance. A controller heats the tray and sample, and during the heating cycle, the weight is measured. Any weight change at certain temperatures is related to the reaction in the sample; this may include decomposition [26]. Any weight loss that occurs throughout the decomposition test is relevant to the amount of polymer that was attached to the particles in the sample.

2.3.3 Scanning Electron Microscope (SEM)

Scanning electron microscopy (SEM) is useful to identify particle size and distribution and to study fracture surfaces. The SEM contains an electron gun creating a source of electrons in an energy range of 1-40 keV. Electron lenses reduce

the diameter of the electron beam and position a small focused beam over the specimen. The electron beam interacts with the near-surface region of the specimen at a depth of approximately 1 μm and it provides signals that will be used to form an image. The resolution of the image improves as the beam size becomes smaller. The SEM device utilized in this work is the Vega 3 from TScan, which is capable of imaging particle detail at approximately 1 nm in accordance with the elemental contrast and other parameters.

To optimize the SEM picture quality and resolution, fine tuning required. In addition, a vacuum is applied in the SEM chamber to reduce the interactions of the beam with gas molecules which affect the image resolution. Non-conductive specimens regularly experience variations in surface potential that introduce astigmatism, instabilities, and false X-ray signals. Charging, a condition of charge collecting on the non-conducting specimen surface inducing excessive brightness, often occurs; this makes it difficult to obtain good quality images. A fine gold layer can be used to sputter coat the non-conductive samples so as to avoid the charging phenomenon [27].

2.3.4 Fourier Transform Infrared Spectroscopy (FTIR)

Fourier transform infrared spectroscopy (FTIR) is useful to analyze the bonding between the polymer matrix and nanoparticles. FTIR estimates the absorption of infrared radiation by the sample material with respect to the wavelength of the radiation. By considering the estimated data, molecular components and structures can be identified. The signal detected is analyzed using Fourier transforms to provide infrared absorption spectra, usually presented as plots of intensity versus wavenumber (in cm^{-1}). Infrared wavelengths absorbed by a material define its molecular structure. The absorption spectrum is in most cases compared against a spectrum from an identified material for detection. Absorption bands in the range of 4000-1500 wavenumbers are generally a result of functional types, such as $-OH$, $C=O$, $N-H$, and CH_3 . The range of 1500-400 is known as the fingerprint region, which usually results from intra-molecular phenomena especially targeted to each material [28].

2.4 Literature review

Chan, et al., 2002 [9] inserted calcium carbonate ($CaCO_3$) nanoparticles in a polypropylene (PP) matrix to examine the nucleation influence of the nanoparticles and their effect on the mechanical properties of the nanocomposite. In their work, the nanoparticles were distributed via melt mixing and obtained an average particle size of 44 nm. Excellent distribution of particles was obtained at 4.8% and 9.2% volume fractions, but many aggregates were found at 13.2%. Nano-sized $CaCO_3$ added to the PP led to an approximately 85-percent improvement in the modulus over the pure PP matrix. A micron-sized $CaCO_3$ addition to the matrix exhibited small improvement to the mechanical properties. They assumed in their study that the increase in the modulus was due to a strong interaction relating to the polymer and filler as a result of the large interfacial area involving them, thereby producing reinforcing and nucleating influences by the $CaCO_3$ nanoparticles. They suggested that the effective interaction and nucleation influences had a counter-balancing force on the mechanical properties. Effective interaction improves the yield strength and tensile strength but it decreases the ultimate strain. However, the strong nucleating influence lowers the size of the spherules, which has the opposite effect, reducing the yield strength and tensile strength but enhancing the ultimate strain. They proposed that the dispersion of nanoparticles is crucial as displayed by the significant effect on the mechanical properties of the reduced volume percent samples, which revealed far better dispersion.

Wang & Zhang, 2012 [29] considered the effect of adding Al_2O_3 to the solvent resistance of PS – Al_2O_3 nanocomposites and its thermal resistance. In addition, they studied the average molecular weight of the PS. Their results showed that the solvent resistance and its thermal resistance improved with the increase of the number of Al_2O_3 nanoparticles. The PS molecular weight in the composites increased with a rise in the Al_2O_3 content.

Ash, et al., 2002 [30] produced PMMA – Fe_3O_4 by combining alumina nanoparticles with synthesized methyl methacrylate, which is compelled by a gas condensing method. They used sonication to spread the particles. They showed that at the most effective percent weight of nanoparticles, the tensile test results revealed

that a 600-percent increase with the %elongation as well as the yield point were obviously obtained. At the same time, the glass transition temperature (T_g) of the nanocomposites decreased to 25°C although the ultimate tensile strength and Young's modulus reduced by 20% and 15%, respectively.

Chen, et al., 2015 [31] manufactured inorganic/organic polystyrene (PS)/ Al_2O_3 nanocomposites by bulk polymerization, and evaluated the mechanical properties of the nanocomposites and investigated the static and dynamic mechanical properties. The static properties were investigated in a tensile test, whereas the dynamic properties were investigated by applying the dynamic storage modulus (E') and the dynamic damping curves $\tan \delta$ (T_g). They stated that the static tensile strength of *PS – nano Al_2O_3* composites was larger than the *PS – micro Al_2O_3* composites. The improvement in strength and modulus was the result of the reinforcement offered by the spread of the Al_2O_3 nano-layers which often create chain formations in the matrix, in addition to conformational influences on the polymer at the Al_2O_3 – *matrix* interface. In contrast, the dynamic results showed that the *PS – Al_2O_3* composites had an improvement on the storage modulus (E') compared to the pure PS. Additionally, the E' for the *PS – nano Al_2O_3* was greater than the *PS – micro Al_2O_3* .

Shelley, et al., 2001 [32] revealed that in the nylon-6 system with 5% weight fraction clay platelets, the modulus improved by 200%, the yield strength improved by 175%, and the ultimate strain slightly reduced. A similar system which has a reduced weight fraction exhibited less improvement in the modulus and yield strength but it revealed a small enhancement in the ultimate strain. The platelets had a surface area of 100 nm², which includes a thickness of 1 nm, and have been found to experience good interaction with the matrix.

Reynaud, et al., 2001 [4] inserted silica nanoparticles of 17, 30, and 80 nm size into a polyamide-6 matrix. In their study, the elastic modulus was larger for the nanocomposites compared to the pure system, but it revealed small variations in particle size. In accordance with the polyamide system given earlier, the yield stress was enhanced with a raising filler concentration and it improved slightly as the size of the particles decreased. The ultimate strain reduced greatly; however, the

concentration increased and the particle size reduced. The research viewed a filler size impact on the filler dispersion and it has revealed a potential presence of an optimum size for the reinforcing particles. They examined the debonding operation to clarify the variations in the mechanical properties relating to the particle sizes. They showed that the 12-nanometer particles typically assembled into aggregates and several debonding process outcomes from debonding around every individual particle. The aggregates, consequently, work like significant soft particles through the deformation process. The 50-nanometer particles were properly distributed and would probably preferentially proceed through a single debonding process. They used the debonding theory to clarify the reason for the increase in the volume of the polymer nanocomposites, with the largest increase occurring in systems while using the smallest particles.

Petrovic, et al., 2000 [14] used nano-sized (10-20 nm) silica fillers to form polyurethane-based composites. They compared the directly-compared mechanical properties of the formed composites with the mechanical properties of the composites created using micron-sized (1.4 μm) fillers. The study provided mixed results. The mechanical and structural properties were seen to be a function of the filler concentration, a 10-to-50-percent weight fraction. Samples with nanoparticles exhibited a more reduced modulus than samples with microparticles at lower than 40% weight fraction, and a larger modulus at 40% and 50% weight fraction. Both nanosilica-filled and microsilica-filled composites revealed a rise in the elastic modulus with the raising filler concentration in the glassy and rubber states. However, the change was expected to have been less in the nanocomposites. The tensile strength improved for the nanocomposites despite being reduced for the microcomposites above 20% weight fraction; there was little difference between the micro- and nano-sized particles below the 20-percent weight fraction. The ultimate strain improved by 600% with the nanofiller; however, it improved only a little with the micro-filler because the glass change temperatures, T_g , were inconsistent. They researched the effect of nanoparticle fillers on composite hardness. Hardness can be a significant property for characterizing elastomers. Hardness was enhanced regularly with microsilica across all concentrations. It was slightly enhanced for nanosilica at lower concentrations after being reduced for large concentrations.

Ash, et al., 2001 [17] conducted mechanical and thermal characterizations of PMMA-alumina nanocomposites with 40-nanometer particles of various concentrations from 0 to 10 weight fraction. The nanocomposites in their investigation were synthesized using free radical polymerization. The elastic modulus for all nanocomposite concentrations was lower than that of the pure PMMA. For the lowest filler content, there seemed to be a sharp initial drop in the elastic modulus followed by a steady rise when the concentration increased; however, it did not approach the amount of the pure system. Additionally, the strain-to-failure for the 5% weight fraction was enhanced by approximately 800% above the pure system. Nevertheless, the ultimate stress of the pure system was greater than the composite. Glass change temperatures reduced by approximately 20°C for the composite systems as compared with the pure system. This decrease in T_g was related to those noticed in the thin films as a function of the film thickness and interfacial properties by which larger chain movability for the interfaces ends in reduced T_g . If the polymers were not bound with the particles, a matrix with various voids would cause a high interfacial area. A system of that category acquires the characteristics of a thin polymer film by having a large surface-to-volume ratio [17].

Rajkumar, et al., 2013 [1] prepared a polymer-nanosilica composite. The reinforcing fillers were silica nanoparticles with Acrylonitrile Butadiene Rubber (NBR). They studied the rheological behavior of the polymer nanocomposite utilizing a rubber process analyzer and produced dispersion for the silica nanoparticles based filler inside the Nitrile Rubber by applying a liquid NBR polymer matrix which they investigated using FTIR, SEM-EDS. They also considered the influence of increasing nanosilica loadings on the mechanical properties of NBR nanocomposites. Their results showed that the NBR/nanosilica based polymer nanocomposites considerably improved the elastic modulus and tensile strength, and produced desirably strong interfaces. In addition, they examined the thermal resistance properties of NBR nanocomposites using air ageing at a 100°C temperature and characterized it using TGA.

Rajkumar, et al., 2013 [1] prepared a polymer-nanosilica composite. The reinforcing fillers were silica nano-particles with Acrylonitrile Butadiene Rubber

(NBR). They studied the rheological behavior of the polymer nanocomposite utilizing a Rubber Process Analyzer. They produced dispersions for the silica nanoparticle based filler inside the Nitrile Rubber by applying a liquid NBR polymer matrix and investigating it using FTIR and SEM-EDS. They also considered the influence of increasing the nano-silica loadings on the mechanical properties of the NBR nanocomposites. Their results showed that the NBR/nano-silica based polymer nanocomposites considerably improved the elastic modulus and tensile strength, and produced desirably strong interfaces. In addition, they examined the thermal resistance properties of the NBR nanocomposites using air ageing at a 100°C temperature and characterized it using TGA.

Sikora, et al., 2016 [33] considered the influence of adding Fe_3O_4 on the mechanical and microstructural properties of cement. The Fe_3O_4 percentage was in the range of 1% to 5%. Their results showed that Fe_3O_4 nanoparticles served to be a filler that enhanced the microstructure of the cementitious composite and lowered its entire porosity, thereby increasing the density of the composite. The existence of nano-magnetite did not change the primary hydration products and the rate of cement hydration. Additionally, the samples, including nano-magnetite, revealed compressive strength enhancement (up to 20%). In their study, the 3 wt. % of nano- Fe_3O_4 in the cementitious composite was the optimal amount to increase both its mechanical and microstructural properties.

Li, et al., 2009 [34] produced a $PMMA - Fe_3O_4$ nanocomposite film using a blend method. They investigated the effect of nanoparticle percentages on chemical structures, mechanical properties, biocompatibility and the surface morphology of the produced $PMMA - Fe_3O_4$ film. They stated that the tensile strength of the nanocomposite films, and its strain, reduced initially and then increased commensurate with the nanoparticle percentage.

Guo, et al., 2007 [35] fabricated vinyl-ester resin polymeric nanocomposites. They utilized unmodified cupric oxide (CuO) nanoparticles which have a bi-functional coupling agent, namely methacryloxypropyl-trimethoxysilane (MPS), to produce the nanocomposites. They observed that the physical properties of the cupric oxide filled the vinyl-ester resin nanocomposite which was significantly affected by

the nanoparticle functionalization. In their study, a comparison was made between the functionalized nanoparticle-filled vinyl-ester resin nanocomposites and the unmodified nanoparticle filled counterparts. The comparison was applied using the thermo-gravimetric analysis (TGA) and they reported that the thermo-stability improved for the modified nanocomposite. Additionally, the tensile test showed an enhancement in the tensile strength for the modified nanocomposite.

Jain, et al., 2006 [36] developed a new method by mixing solid-state modification (SSM) resulting from the grafting of vinyl triethoxysilane (VTES) with a sol-gel approach to create PP/silica nanocomposites using various degrees of adhesion between the filler and matrix. They grafted VTES using SSM in porous PP particles. Bulk polymerization was tested producing homo-polymerization of VTES and these tests were applied under the same experimental conditions as SSM. They utilized size exclusion chromatography (SEC) and nuclear magnetic resonance spectroscopy (NMR) experiments and reported that the VTES was grafted forming one monomeric unit in the amorphous phase of the PP with the probability for VTES-polymer grafting in the course of the SSM. They applied the sol-gel method to synthesize in-situ silica-like nano-particles. In addition, they conducted the magic-angle spinning $MAS^{29}Si$ NMR spectra. These tests revealed that the silica-like chemical blocks were O_3 and O_4 . The grafted VTES became part of the in-situ produced silica particles as concluded from the $MAS^{29}Si$ NMR and FTIR spectroscopy. The TEM and SEM showed that the in-situ produced silica particles were generally close to being spherical with sizes ranging from 50 to 100 nm.

Nabid, et al., 2008 [37] provided an enzymatic method to insert nanocomposites between Polyaniline (PANI) and anatase (TiO_2) nanoparticles (NPs). They reported that the sulfonated polystyrene (SPS) occurrences had an impact on the polymerization reaction. Their proposed method used horseradish peroxidase (HRP) to catalyze the polymerization. In addition, it deposited the polyaniline onto the surface of the TiO_2 NPs creating a core-shell composition. FTIR spectroscopy, UV-Vis. spectroscopy and scanning electron microscopy (SEM) were used to characterize the enzymatically synthesized nanocomposite. They reported a presence of strong interactions in the interface of PANI and the nano- TiO_2 . They

concluded various changes in the values of the peak potentials for anodic, cathodic and formal potentials for PANI/ TiO_2 NPs (39 mV and 591.5 mV, respectively) and PANI (281 mV and 425.5 mV, respectively).

Lau and Piah, 2011 [38] reviewed the influence of the electrical discharges which induced the surface tracking and partial discharge phenomena relating to polymer nanocomposites. They reported that obtainable knowledge concerning tracking attributes of polymer nanocomposites was very limited, and that the experimental results provided were generally scanty. Alternatively, the majority of the partial discharge activities focused on surface discharge evaluation methods. Inner discharge attributes of polymer nanocomposites were not effectively researched. Nevertheless, if the utilization of polymer nanocomposites could actually improve the tracking and internal discharge attributes, it should still be investigated.

Momeni and Pakizeh, 2013 [39] fabricated membranes using polysulfone (PSf) that contain magnesium oxide (MgO) nanoparticles together with gas permeation characteristics. They prepared the membranes by mixing a solution together with the phase inversion technique. Membrane morphology, void creation, and the distribution and aggregation of MgO were seen by SEM. Additionally, they applied a thermal gravimetric analysis (TGA) test to examine the thermal stability of the membranes, membrane film residual solvent and membrane structural breakdown. Differential scanning calorimetry (DSC) was used to assess the influence of MgO nanoparticles on the glass change environment (T_g) and it was shown that the T_g membranes improved with MgO additives. The bonds variation was inspected using Fourier transform infrared (FTIR) spectra. Their results showed that the permeability increased with the addition of MgO nanoparticles to the polymeric membrane.

CHAPTER THREE

EXPERIMENTAL WORKS

3.1 Introduction

This chapter describes the experimental procedures conducted in this work in addition to the samples preparation procedures for all tests and the tests performed on those samples, including tensile tests, TGA, SEM and FTIR.

3.2 System initial mixture

Four polymer nanocomposite systems were synthesized and the same procedure was followed for the two pure reference polymer systems. Adequate amounts of solution for each system were produced initially to help the synthesizing of specimens for each mechanical characterization and analytical technique. To obtain 5% filler weight fraction in a 15% polymer weight fraction (to solvent) solution, the system portions for the four polymer nanocomposite systems were computed. A 30-percent polymer weight fraction solution was achieved for the two reference polymer systems. The nanocomposite systems were set as lower weight fraction solutions to give a less viscous environment into which the nanoparticles could be distributed.

Table 3-1 shows the levels of each element used to synthesize the primary mixtures. All samples were mixed and stored in 500-milliliter Erlenmeyer flasks. Before employing all the equipment in the laboratory, such as flasks, stirrers, spatulas, slides, etc., they were washed with Alconox soap and water, rinsed with acetone along with the correct solvent, and then put into a Fisher Scientific Isotemperature dry oven for approximately 20 minutes at 100°C until dry.

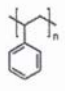
Polystyrene PS pellets, with $400,000 \frac{g}{mol}$ weight averaged molecular weight (\bar{M}_W) and $1.032 g/cm^3$ density, was obtained from the Aldrich Chemical Company, Inc. The poly(methyl methacrylate) PMMA granules, $M_W = 400,000 g/mol$, $1.210 g/cm^3$ density, were obtained from the Aldrich Chemical Company. Figures 3-1 and 3-2 show the specifications of the PMMA used in the present work. The density of the alumina and magnetite was $4.00 g/cc$ and $5.15 g/cc$, respectively; their specifications as nanoparticles are shown in Figures 3-3 and 3-4. Toluene (density $0.867 g/cc$) obtained from Fisher Scientific was used as a solvent for all polystyrene PS-based systems. Chlorobenzene 99+% (density $1.106 g/cc$) was used as the solvent for all poly(methyl methacrylate) PMMA-based systems.

Table 3-1 Constituents used to make polymer nanocomposite systems

System	Polymer (ml)	Filler (g)	Solvent (ml)
PS (pure/reference)	36.33	–	140
PS-Fe ₃ O ₄	50	0.5	385
PS-Al ₂ O ₃	40	0.5	308
PMMA (pure/reference)	32.48	–	110
PMMA-Fe ₃ O ₄	40	0.5	247
PMMA-Al ₂ O ₃	30	0.5	203

SIGMA-ALDRICH sigma-aldrich.com

3050 Spruce Street, Saint Louis, MO 63103, USA
 Website: www.sigmaaldrich.com
 Email USA: techserv@slal.com
 Outside USA: eurtechserv@slal.com



Polystyrene

-
-
-
- Synonym: PS
-
-
- Linear Formula: $[CH_2CH(C_6H_5)]_n$

Figure 3-1 PS (pure/reference) Matrix specifications

SIGMA-ALDRICH sigma-aldrich.com

3050 Spruce Street, Saint Louis, MO 63103, USA
 Website: www.sigmaaldrich.com
 Email USA: techserv@slal.com
 Outside USA: eurtechserv@slal.com

Product Specification

Product Name: Poly(methyl methacrylate) - average M_w -120,000 by GPC

Product Number: **182230**

CAS Number: 9011-14-7

MDL: MFCD00134349

Formula: $(C_5H_8O_2)_n$



TEST	Specification
Appearance (Color)	White
Appearance (Form)	Powder or Crystals
Infrared spectrum	Conforms to Structure
Viscosity c = 29%-31% in Toluene/Butanol 90:10	250 - 500 cps

Specification: PRD.0.Z05.10000022085

Figure 3-2 PMMA (pure/reference) Matrix specifications

SIGMA-ALDRICH		sigmaaldrich.com	
		3050 Spruce Street, Saint Louis, MO 63103, USA	
		Website: www.sigmaaldrich.com	
		Email USA: techserv@sls.com	
		Outside USA: eurtechserv@sal.com	
Product Specification			
Product Name: Iron(III) oxide - nanopowder, 50-100 nm particle size (SEM), 97% trace metals basis			
Product Number:	637106	Fe_3O_4	
CAS Number:	1317-61-9		
MDL:	MFC00011010		
Formula:	Fe ₃ O ₄		
Formula Weight:	231.53 g/mol		
TEST	Specification		
Appearance (Color)	Black		
Appearance (Form)	Powder		
Titration by Na ₂ S ₂ O ₃			
% Fe	Conforms		
Particle Size	Conforms		
50-100 nm (SEM)	Confirmed		
ICP Major Analysis	Confirmed		
Confirms Iron Component	Conforms		
Purity	Conforms		
97% Based On Trace Metals Analysis			
Trace Metal Analysis	≤ 35000.0 ppm		
Specification: PRD.3.Z05.10000005630			
<small> (Revised) 06/23/05 10000005630 10000005630 ALL INFO ON THIS PRODUCT US01 ©2005 SIGMA-ALDRICH </small>			

Figure 3-3 Fe_2O_3 nanoparticle specifications

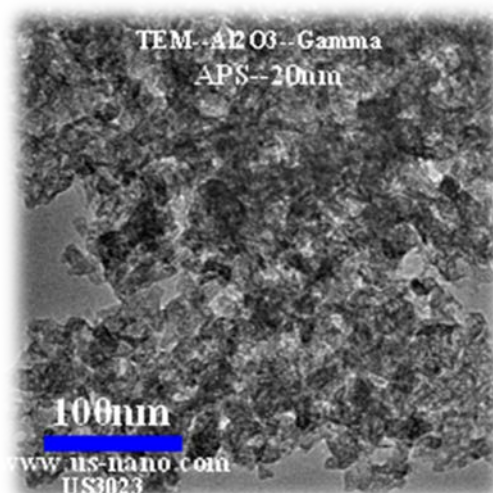


Figure 3-4 Specifications of Al_2O_3 nanoparticles.

Identical techniques were used to prepare samples for every system. The PS- Fe_3O_4 samples were made using the following strategy: A 1000-milliliter flask, a volumetric cylinder, a spatula, and a stirrer were set as described earlier. A 385-milliliter aliquot of toluene was measured and put into the flask. The flask was positioned on a Thermocline Miraka mixing hotplate at a 60°C temperature and 500 rpm. A magnetic stirrer was placed inside the flask and started spinning. 50 ml

of polystyrene PS was measured and put into the flask with the toluene. At first, the polystyrene PS shaped a viscous layer at the bottom of the flask. The flask temperature rose to 80°C. Immediately after 3 hours, the mixture became clean and the stirrer was spinning freely, showing that the polymer dissolved. The stirrer was pulled from the flask and 0.5 grams of magnetite was measured and placed on some weighing paper. While the mixture was circulating continuously, the magnetite was gradually mixed in the flask, which continued for 10 minutes. The flask was covered with can parafilm “M” laboratory film and placed under a fume lid.

Other systems were prepared following the same strategy previously mentioned using certain modifications in applied temperatures and within the time needed to dissolve. All of the testing samples were made from the solutions synthesized from the techniques shown previously.

3.3 Tests and inspection

In this section, the following tests applied in this work will be described: the tensile test, Thermal Gravimetric Analysis (TGA), Scanning Electron Microscopy (SEM) and Fourier Transform Infrared Spectroscopy (FTIR).

3.3.1 Tensile test

Tensile testing was applied to determine mechanical properties such as elastic modulus, yield stress, ultimate tensile strength, etc. To prepare samples for the tensile test, some important items are required. The samples for the six systems were constructed using the same procedure even though variations were applied to achieve good sample quality. The tensile test samples were manufactured from the mixtures prepared in advance. They are shaped like a ‘dog bone,’ as shown in Figures 3-5(a) and (b). The main concern in constructing the sample was the removal of the solvents and ensuring that no air pockets were in the neck region of the samples. Many samples were manufactured for each system.

Four aluminum molds were designed and manufactured according to ASTM D638. The molds have dimensions of 180 mm × 50 mm × 20 mm and contained

removable top, bottom, and middle pieces. The sample dimensions are of type I in ASTM D638, as shown in Figure 3-6.

In the top and bottom sides of the molds, notches were made to simplify the extraction of a hardened sample. The areas of each mold that will contact the sample are sprayed with a mold release agent, Sprayon Dry Film P. T. F. E, before using the mold. The mold release agent simplified the removal of the hardened samples.

After the mold is sprayed and left to dry, the top part of the mold is removed and the mold is placed on a level surface. The sample is poured into the mold until it is full with the solution. The solution is left for 48 hours while the solvent evaporates. Even after the solvent has evaporated, air bubbles are observed in all samples, as seen in Figure 3-7. To overcome this phenomenon, the filling procedure is performed layer by layer. The first layer is poured into the mold at an approximate thickness of 1 mm and left for 48 hours; then it is pressed using a punch design with a clearance of approximately 0.5 mm on each side. The pressing force at this stage is applied by hand. After the sample layers reach the specified thickness given in ASTM D638 and to increase the solvent evaporation, the mold is placed in an oven at a temperature of between 100° and 120°C.

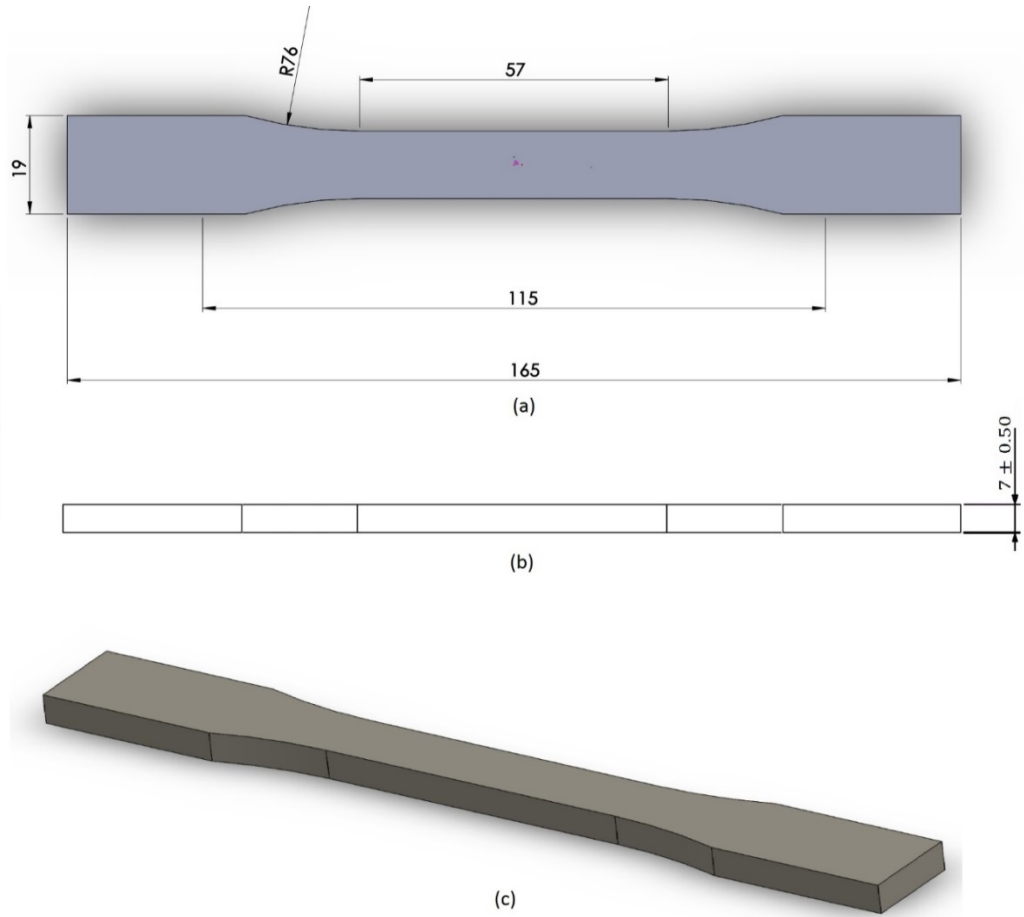


Figure 3-5 Tensile test sample (a) Top view (b) Side view (c) 3D view

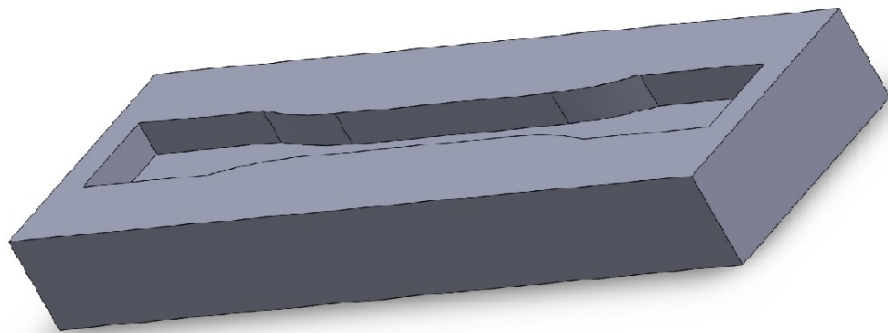
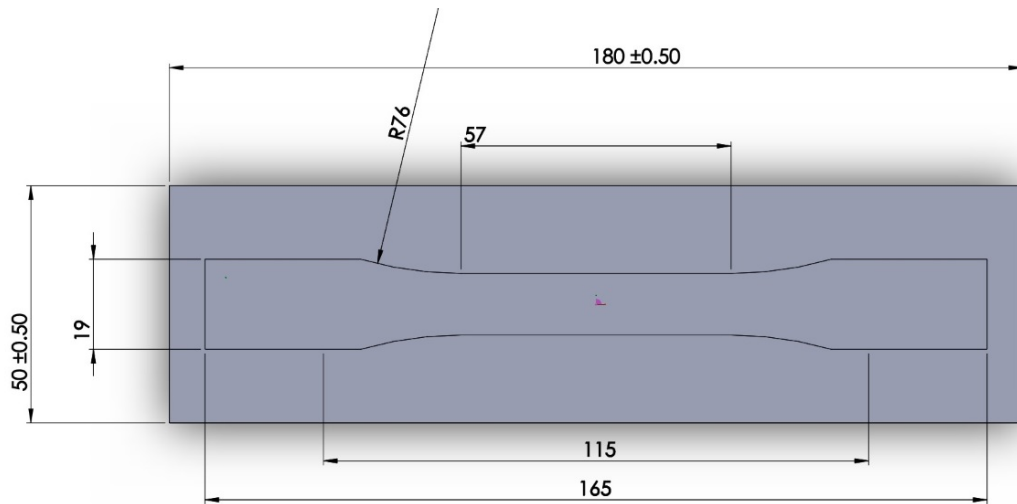


Figure 3-6 The designed mold



Figure 3-7 Air bubbles in manufactured samples

After 48 hours, the solvent evaporates inside the dry oven and the samples are placed into a vacuum oven to remove the remaining solvent. They are kept warm during the transformation in the preheated vacuum oven at $100^{\circ} - 160^{\circ}\text{C}$ for between 48 and 72 hours. The mold is left in the vacuum oven at (1500 *kPa*). The dog bone tensile test samples at this time are free from the solvent. After that, the

mold pulled up from the vacuum oven, and the sample is re-pressed while it is warm to increase the layer bonding and to reduce the likelihood of air bubbles.

The samples are extracted from the mold slowly and carefully. The edges of the samples are smoothed using emery. The dimensions of every sample are measured using a micrometer with an accuracy of $0.1 \mu m$. The colors of the samples are dark brown and slightly translucent light yellow for the magnetite and aluminum samples, respectively.

Figure 3-8 shows a cross section of the assembled mold, sample and punch system used in this work to manufacture the tensile specimens. Figure 3-9 shows the transparent assembly and the completed tensile test specimen prior to being extracted from the mold.

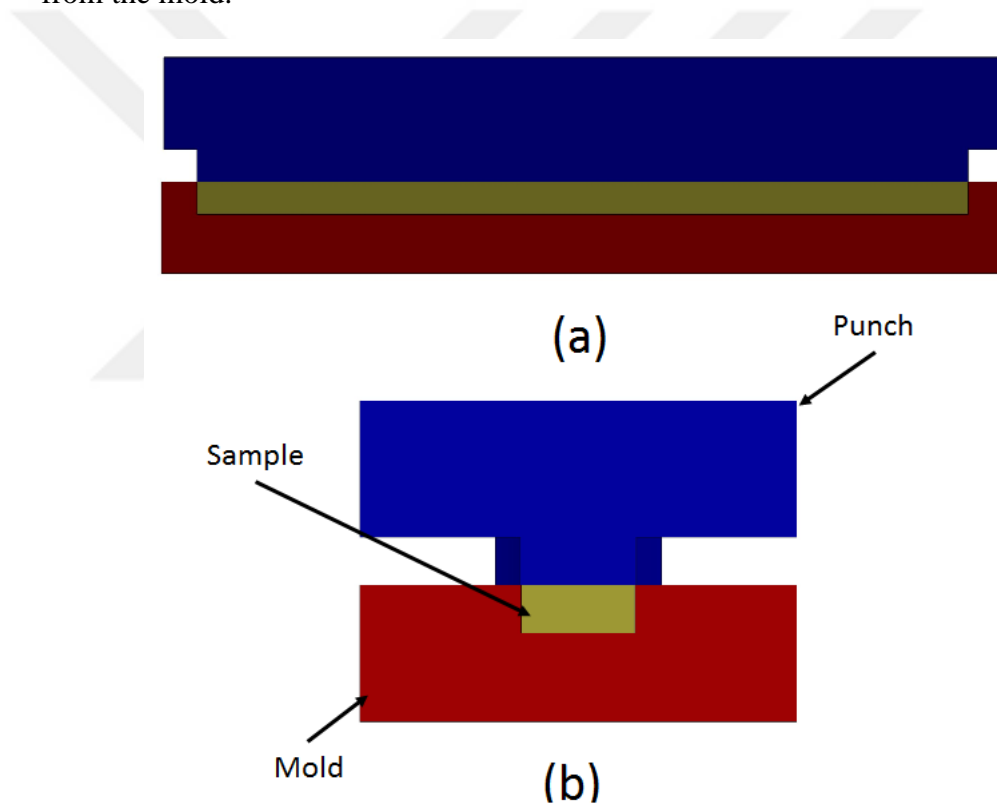


Figure 3-8 Cross section of mold, sample and punch assembly

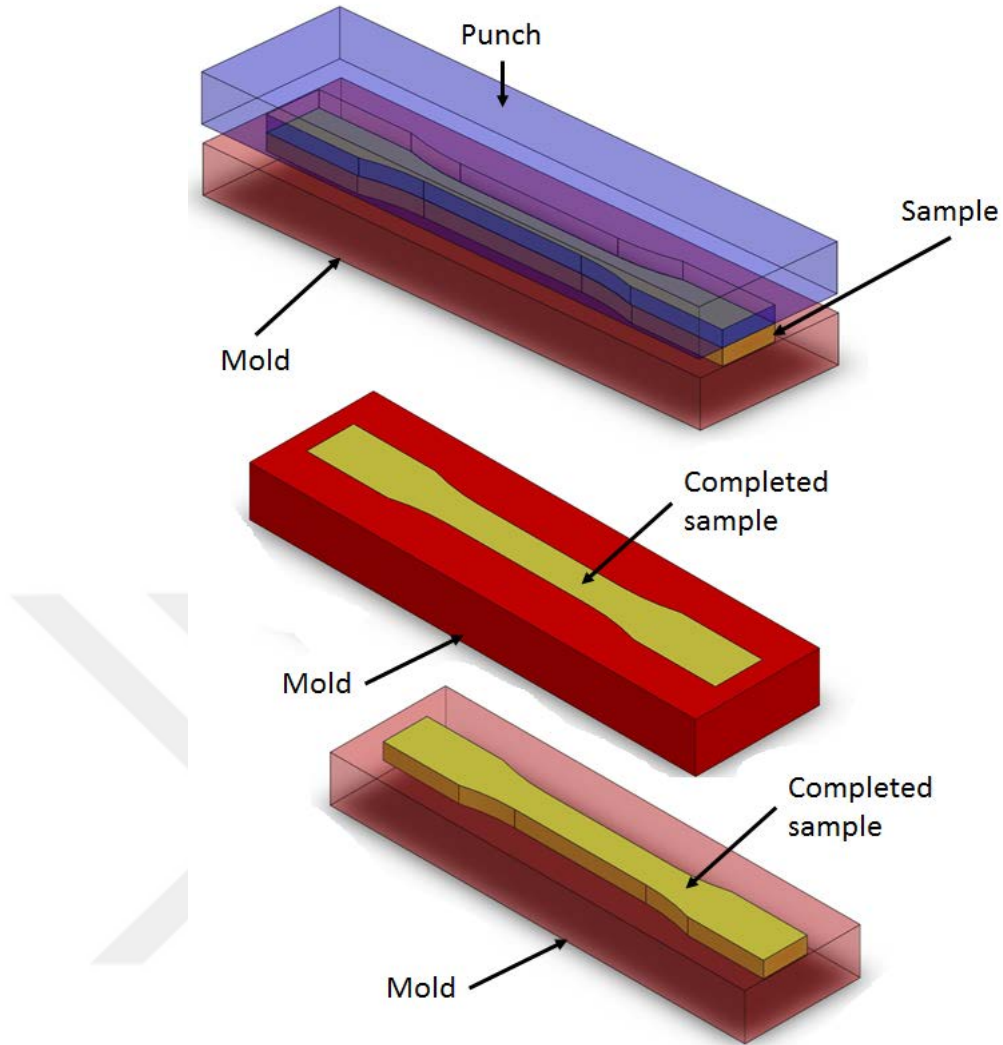


Figure 3-9 Mold, sample and punch assembly

As seen in Figure 3-10, a tensile test machine at the Material Engineering Department, University of Technology in Baghdad, Iraq, namely the WDW-200e, is utilized to examine every sample. It is a computerized instrument with maximum load of 20 KN. An extensometer is used to measure the strain. Before the machine and its extensometer are used, they need to be calibrated. Two-sided tape is twisted across the sample in the location where the extensometer is fitted. Elastics and heavy rubber bands are used to secure each end of the extensometer to avoid slipping.

The cross head speed applied in the test was 2 mm/min. The machine measures the displacement, load and time. The software supplied with the machine

computes the tensile test results and stores each test datum in a separate file. The data stored include the stroke speed, change in length (displacement), time, load, engineering stress, engineering strain, true stress, true strain, ultimate strength modulus of elasticity, and so on.



Figure 3-10 The WDW-200e Tensile Test Machine

The software performs its computations according to the following standard tensile test equations:

$$e = \frac{\Delta L}{L_0} \quad (3-1)$$

$$\sigma_e = \frac{F}{A_0} \quad (3-2)$$

where, e is the engineering strain, ΔL is the change in length in mm , the sample gauge length L_o in this work is equal to 50 mm (the distance between the extensometer ends), σ_e is the engineering stress (MPa), F is the applied force in (N) and A_o is the initial cross section area of the sample in mm^2 . Other equations and calculations that the software can perform that were not mentioned because they are not used. The ultimate tensile strength is the maximum point on the test results before fracture. Six samples were tested for each composite system and the average is taken.

The true stress can be computed by dividing the applied force by the actual area, which can be calculated using a constant volume role. The sample volume remains constant through the test, which means

$$A_o L_o = AL$$

$$A = \frac{A_o L_o}{L} \quad (3-3)$$

$$L = L_o + \Delta L \quad (3-4)$$

where, A_o is the original area, L_o the original length, A the instantaneous area and L the instantaneous length. The true stress will be

$$\sigma = \frac{F}{A} \quad (3-5)$$

$$\epsilon = \ln\left(\frac{L}{L_o}\right) \quad (3-6)$$

where σ is the true stress and ϵ the true strain.

The modulus of elasticity E is the slope of the linear portion of the stress-strain curve and is computed thus,

$$E = \frac{\sigma_e}{e} \quad (3-7)$$

In addition, the percentage elongation is computed as follows:

$$\%e = \frac{\Delta L_{max}}{L_o} \times 100 \quad (3-8)$$

3.3.2 Thermal Gravimetric Analysis (TGA)

TGA is utilized to determine the effect of the presence of nanoparticles on the decomposition temperature and to assess the thickness of the polymer layer adsorbed into the nanoparticles. Two types of samples were prepared for the TGA. To identify decomposition temperatures and polymer layer thickness, thin film samples on slides and samples of polymer capped nanoparticles were prepared, respectively.

The TGA samples preparation procedure is applied in all systems as follows: As mentioned in the tensile test sample preparation, there were some air bubbles. Therefore, the same procedure that followed was applied. The solution was poured onto a level glass slide to fill the surface of the major slide and left to harden for approximately 48 hours while the solvent evaporated. The solution was pressed to avoid air bubbles after that period. Then, the glass was placed into an oven at a temperature of $100 - 120^{\circ}\text{C}$ for approximately 48 hours without vacuum to help the solvent to evaporate. Afterwards, the samples were placed into a $100 - 160^{\circ}\text{C}$ preheated vacuum oven at 1500 kPa to remove any remaining solvent. The vacuum was removed after 15 hours and the oven left to cool to room temperature normally. The thickness of the produced samples on the glass slide was $0.5 - 1.5\text{ mm}$. In order to fit the sample into the TGA pan, a cutter was used to cut small pieces from the produced samples.

TGA capped nanoparticle samples were prepared by following two methods. Each of these techniques includes pouring a 30-40-milliliter aliquot of the initial system mixture into a set vial. The aim of each of these methods was to separate the extra polymer and solvent in the polymer-coated nanoparticles. It was observed that the precipitation of particles in the solution started after a short time. The closed vial which was filled with the mixture was left without moving it for 48 hours; as a result, a layer of precipitated capped particles formed at the bottom of the vial. The liquid part of the vial was poured out and removed, at all times being careful not to drop any particles. The vial was refilled with solvent and shaken using a vibration machine for 2 minutes to remove any additional unbound polymer in the particles. The closed vial was stored without disturbing it for a further 48 hours whilst the layer of precipitated capped nanoparticles forms at the bottom of the vial. This procedure

is repeated 6 times so that the final solution includes only the solvent and fine particles without any observable excess polymer.

The second approach is to prepare capped particle samples implemented in a centrifugal machine in order to accelerate particle precipitation. The particles in the vial are spun at 12,000 rpm for 20 minutes.

The capped particles form a solid mass at the bottom of the vial. The extra polymer and solvent solution is removed and the other particles are washed with solvent to remove any additional unbound polymer. The vial is vibrated with a vibration machine for 4 minutes to remove any additional unbound polymer within the particles. This procedure is repeated 5 times. It should be mentioned that both techniques produce identical TGA results. For each test, the pan was cleaned using soap and water and any visible residue was removed.

The thin film sample average sizes were 10 mg, whereas the capped particle samples were 3 mg. Prior to undertaking any TGA tests, the device is weight calibrated based on the instructions supplied by the manufacturer. The software results are time, temperature, and weight for over 2000 points through the temperature range.

3.3.3 Scanning Electron Microscopy SEM

The distribution of particles and their size in the tensile test samples are considered using the SEM. To stabilize the samples on a sample holder, carbon tape is used under the sample and a small carbon tape roll is rolled around the sample. Due to the polymers being non-conductive and possibly encountering charging in the SEM, the samples are sputter coated with gold utilizing a sputter coater.

The layer of thin gold atoms that are used to cover the samples eliminates the charging effect. The sputter coater chamber is evacuated at 100 Pa, followed by the samples being sputtered coated for approximately 90 seconds to reduce the thickness of the gold layer and consequently reducing the surface characteristic distortion.

The SEM being used was a TScan Vega 3 Scanning Electron Microscope at 30 kV and various images of each sample are obtained. These images are processed

using the Vega 3 software, which provides measuring tools to determine directly the particle size++.

3.3.4 Fourier Transform Infrared Spectroscopy (FTIR)

Fourier Transform Infrared Spectroscopy (FTIR) is used to analyze the bonding between the polymer matrix and nanoparticles. FTIR measures the absorption of infrared radiation by the sample material with respect to the wavelength of the radiation.

The Fourier Transform-Infrared Spectroscopy (FTIR) device at the Material Engineering Department, University of Technology in Baghdad, Iraq (Figure 3-11) is an analytical device used to identify organic (and in some cases inorganic) materials. This technique measures the absorption of infrared radiation by the sample material versus wavelength. The infrared absorption bands identify molecular components and structures.

When a material is irradiated with infrared radiation, the absorbed FTIR radiation usually excites molecules into a higher vibrational state. The wavelength of light absorbed by a particular molecule is a function of the energy difference between the at-rest and excited vibrational states. The wavelengths that are absorbed by the sample are characteristic of its molecular structure.

The FTIR spectrometer uses an interferometer to modulate the wavelength from a broadband infrared source. A detector measures the intensity of transmitted or reflected light as a function of its wavelength. The signal obtained from the detector is known as an interferogram, which must be analyzed with a computer using Fourier transforms to obtain a single-beam infrared spectrum. The FTIR spectra are usually presented as plots of intensity versus wavenumber (in cm^{-1}). The wavenumber is the reciprocal of the wavelength. The intensity can be plotted as the percentage of light transmittance or absorbance at each wavenumber.



Figure 3-11 Fourier Transform Infrared Spectroscopy (Perkin Elmer Spectrum 100)

FTIR is used to discover the bonding between the polymer matrix and the nanoparticles. Examining spectra requires comprehensive knowledge of which peaks indicate which bonds. Bonds between the matrix and nanoparticles for PMMA based samples are expected, and FTIR is applied for two PMMA based samples only.

The Spectra Tech liquid demountable cell with a 0.2 millimeter Teflon spacer and KBr windows are disassembled, cleaned with wipes and solvent, and reassembled. This procedure occurs prior to running any FTIR test. The cell is placed into the FTIR spectrometer, and as soon as the infrared sample compartment is sealed and cleared for at least 6 minutes, a background spectrum is utilized and designated for use on the following spectra acquisitions.

The vials filled with the centrifuged capped particles are shaken to re-suspend the particles. A non-reusable pipette is utilized to move an aliquot of the capped particle suspension to the cell, ensuring that no air bubbles remain in the cell. The cell is placed into the spectrometer and the sample compartment is sealed and purged for at least 6 minutes. The sample spectrum is obtained and stored for further analysis. The spectrum is compared with a formerly recorded spectrum of PMMA and chlorobenzene solvent. By comparing specific capped particle peaks with PMMA-chlorobenzene peaks, bonding distinctive to the capped particles is highlighted. The specific peak wavenumber and baselined peak heights are analyzed.

CHAPTER FOUR

RESULTS AND DISCUSSION

4.1 Introduction

This chapter describes the results collected from the tests conducted in this work. These tests are mentioned in Chapter Three: the tensile test, TGA, SEM and FTIR. The data are divided into two groups depending on their based material, the first group being PMMA and the second being PS.

4.2 Tensile Test Results

Tensile tests were carried out to estimate the mechanical properties of the polymer nanocomposites. There are many parameters affecting the polymer mechanical properties such as molecular weight, tacticity, and processing history. Therefore, the pure polymer reference systems were tested to be compared directly with the nanocomposites.

The tensile instrument measures the sample resistance load generated from the sample extension. As mentioned in Chapter 3, the tensile test is conducted using a 2 millimeter-per-minute cross head speed. The load extension curves are shown in Figures 4-2 and 4-3 for the PMMA and PS groups, respectively. The engineering stress strain curves are computed using Equations 3-1 and 3-2. Figures 4-4 and 4-5 show the engineering stress-strain curves for the PMMA and PS groups, respectively. Figures 4-6 and 4-7 show the true stress-true strain curves for the PMMA and PS groups, respectively. The computed tensile properties are given in Table 4-1 for the PMMA group and in Table 4-2 for the PS group. It is clear that the modulus of elasticity E for both reference systems is higher than the system with additives. In

addition, the ultimate tensile strength for the system with the Al_2O_3 additive is higher than the reference and Fe_3O_4 additive systems. Table 4-3 shows the percentage change in ultimate tensile strength $\% \Delta \sigma_{ult}$ and the percentage change in ultimate strain $\% \Delta e_{ult}$. It can be seen that the systems with Al_2O_3 provide enhancement for ultimate tensile strength, % elongation and the ultimate strain. In contrast, the systems with Fe_3O_4 have lower ultimate tensile strength and some increase in the %e and $\% \Delta e_{ult}$. From these results, the addition of Al_2O_3 for both groups provided, to a certain degree, enhancement better than those with Fe_3O_4 . The results of the Al_2O_3 additive for the PMMA composite agree with those of Ash, et al., [17] such that the tensile strength and % elongation increased, but the modulus of elasticity is reduced in contrary to the results of [17]. Ash, et al., in their second study [30], showed that the 5% filler reduces the modulus of elasticity and tensile ultimate strength, whereas the % elongation increases. They reported that the main failure mode of PMMA is by crazing, which leads to brittle failure. They observed that the failure of the surface morphology of the synthesized unfilled PMMA displays features of failure by craze formation and growth as expected. They proved that the method of yielding for the PMMA has been altered and a brittle-to-ductile yielding change occurs. Similar results were given by Chen, et al., [31], where the tensile strength and the % elongation for the PS system increases with the Al_2O_3 additive, whereas the modulus of elasticity is reduced in contrast to the results given in [31]. The improvement in strength is due to the reinforcement supplied by the distributed Al_2O_3 nano-layers, which often gives rise to a chain formation in the matrix in addition to conformational influences on the polymer at the Al_2O_3 -matrix interface. This increase is due to the nanoparticles being present with minimum bonding with the neighboring matrix, thereby causing expansions into the voids when the tensile stress is applied, relieving the generating triaxial stress and avoiding craze void creation and early failure [17] [30] [31].

It should be mentioned that the addition of Fe_3O_4 to the PMMA produces similar results in Li, et al., [34] with the same weight percentage of Fe_3O_4 . As mentioned in Ash, et al., [30], considering the mechanical properties of the pure PMMA and the effect of adding 5% weight of nano Al_2O_3 filler: the addition of

nano- Al_2O_3 filler has little effect on the free-radical polymerization of the PMMA. The stress-strain curve from their results is shown in Figure 4-1. It can be seen that the addition of nano Al_2O_3 reduced the modulus of elasticity, the yield stress and the ultimate tensile strength, whereas the % elongation increased. They reported that the primary mode of failure for the pure PMMA is by crazing, which leads to a brittle failure. In contrast, the nanocomposites fracture surfaces did not show any craze formation attributes or propagation. A brittle-to-ductile transition (BDT) occurs with the yield phenomenon and the ultimate failure is attributable to brittle-type fast fracture. The transition is a result of the ability of polymer chains to change their local formation and eliminate the applied triaxial stress. This may occur prior to void formation and following crazing.

To sum up, one may expect that the addition of nanoparticles, either Al_2O_3 or Fe_3O_4 , in both polymers systems (PS and PMMA), would enhance mechanical properties. However, the modulus of elasticity and perhaps the yield stress values decreased (Figures 4-4 and 4-5). As mentioned above, similar results were also observed in [30].

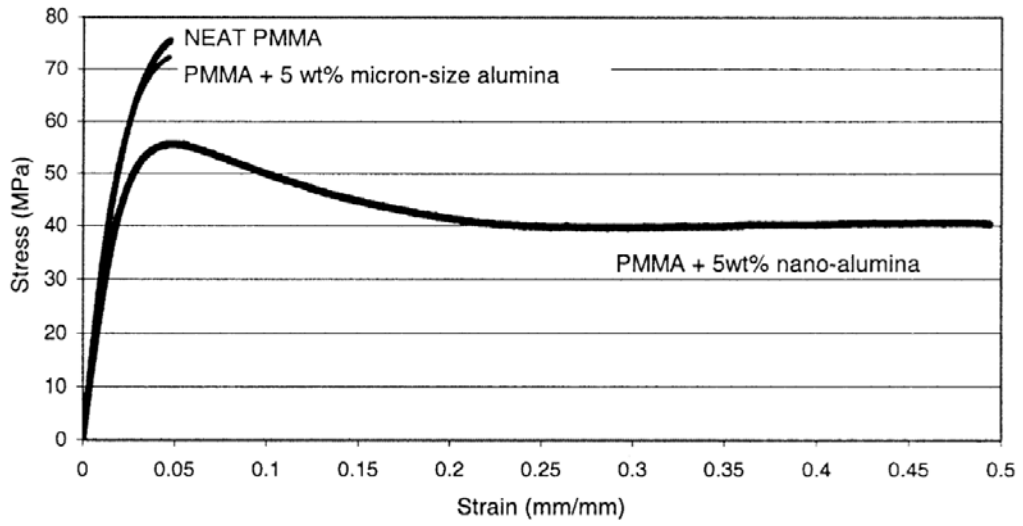


Figure 4-1 Stress-strain curve for different materials from Ash et al., [30]

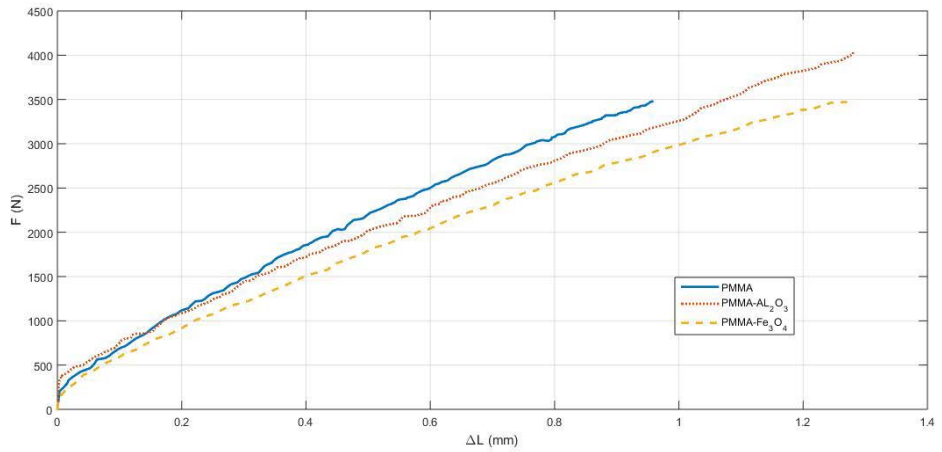


Figure 4-2 Load-extension curves for the PMMA group

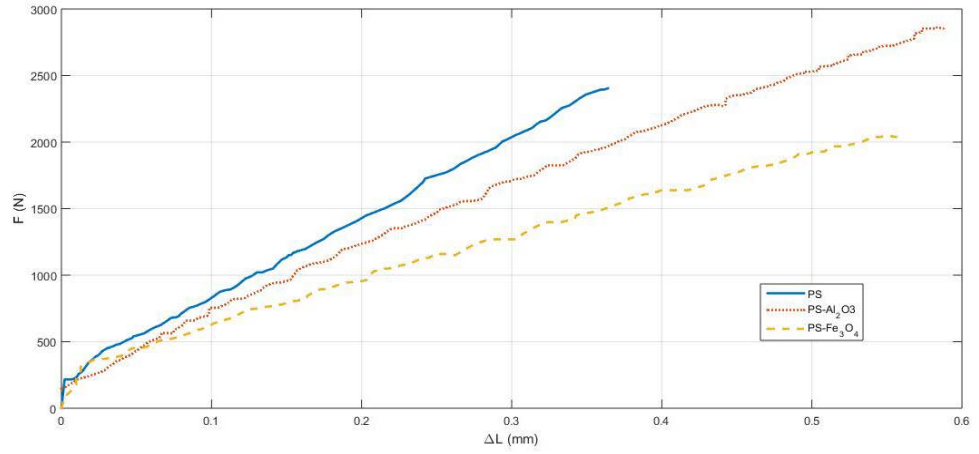


Figure 4-3 Load-extension curve for the PS group

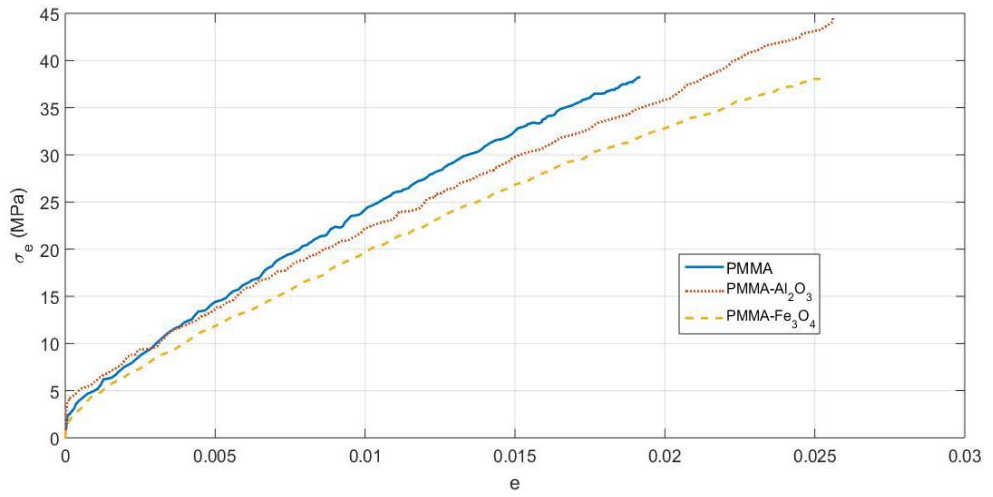


Figure 4-4 Engineering stress strain curves for the PMMA group

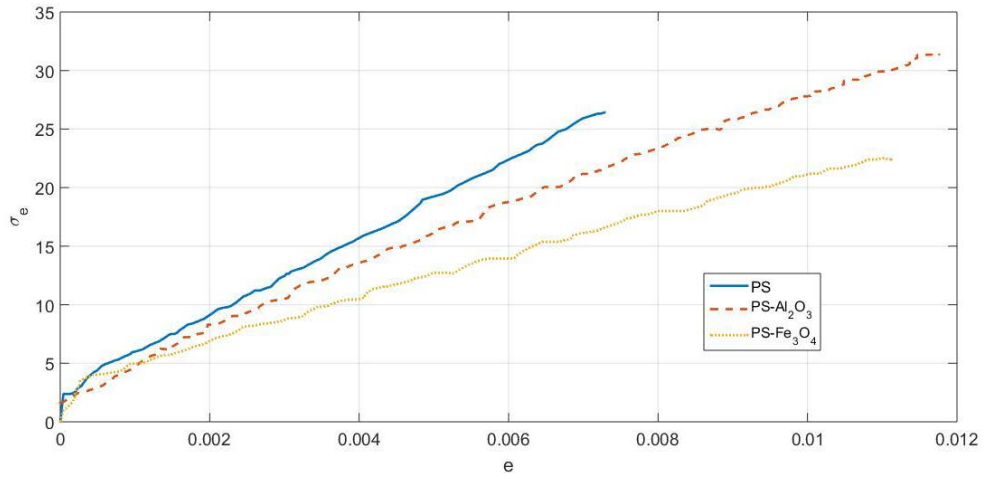


Figure 4-5 Engineering stress strain curves for the PS group

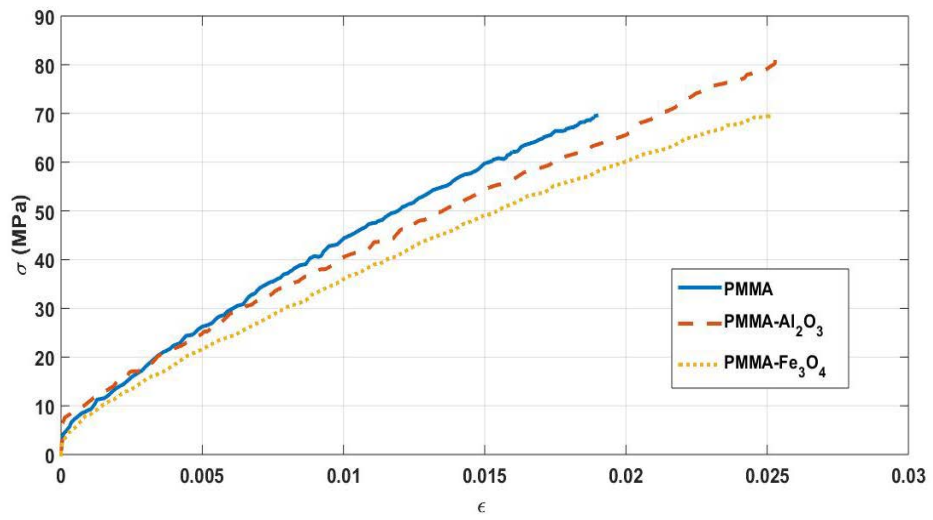


Figure 4-6 True stress-strain curves for the PMMA group

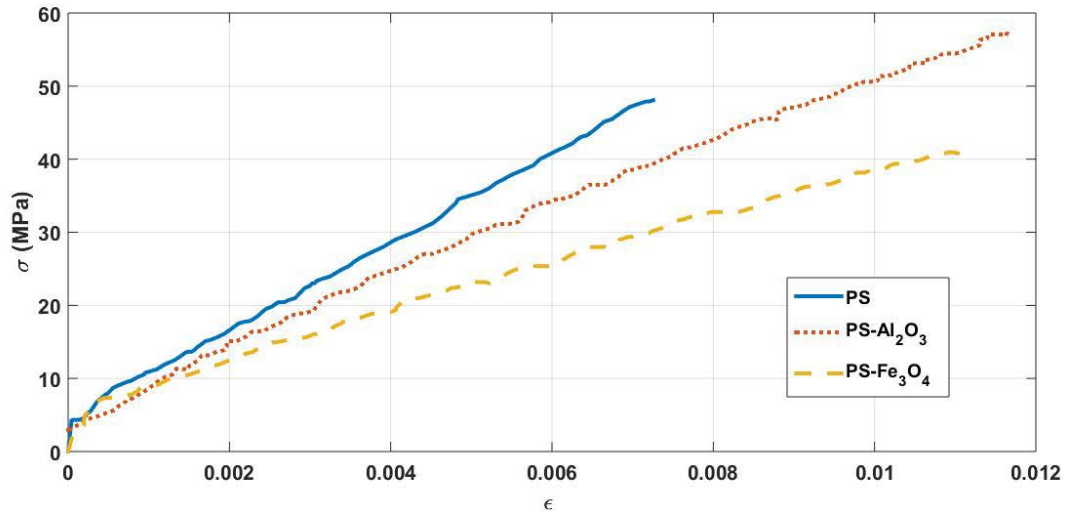


Figure 4-7 True stress-strain curves for the PS group

Table 4-1 Tensile test mechanical properties for the PMMA group

System	E (GPa)	σ_y (MPa)	σ_{ult} (MPa)	e_{ult}	%e
PMMA	2.8103	13.69	38.22	0.01915	1.9146
PMMA – Al_2O_3	2.6326	12.6	44.52	0.02560	2.650
PMMA – Fe_3O_4	2.5852	10.17	38.15	0.02538	2.528

Table 4-2 Tensile test properties for the PS group

System	E (GPa)	σ_y (MPa)	σ_{ult} (MPa)	e_{ult}	%e
PS	3.7528	7.436	26.42	0.007282	0.7232
PS – Al_2O_3	3.2692	6.169	31.46	0.011760	1.1760
PS – Fe_3O_4	2.9664	5.786	22.4	0.011120	1.1118

Table 4-3 Change in ultimate strength and strain

System	$\Delta\sigma_{ult}$	% $\Delta\sigma_{ult}$	e_{ult}	% Δe_{ult}
<i>PMMA</i>	38.22	--	0.01915	--
<i>PMMA – Al₂O₃</i>	44.52	16.483	0.02560	33.681
<i>PMMA – Fe₃O₄</i>	38.15	-0.183	0.02538	32.532
<i>PS</i>	26.42	--	0.007282	--
<i>PS – Al₂O₃</i>	31.46	19.0765	0.011760	61.49
<i>PS – Fe₃O₄</i>	22.4	-15.216	0.011120	52.7

The Al₂O₃ nanoparticle additives with the two polymer systems (*PMMA – Al₂O₃* and *PS – Al₂O₃*) produced improvements in the mechanical properties (ultimate tensile strength, % elongation (e) and the ultimate strain Δe_{ult}) for the pure polymer PMMA and PS system, whereas the two polymer systems with Fe₂O₃ nanoparticles additives resulted in worse mechanical properties for the polymer nanocomposite reinforcement by Fe₃O₄ nanoparticles.

4.3 Scanning Electron Microscopy (SEM)

The main objective of applying SEM is to obtain particle sizes for the interphase analysis and to estimate particle dispersion. SEM images are determined for the tensile test specimen fracture surfaces of all four nanocomposite systems. The fracture surfaces are sputter coated with gold atoms prior to imaging in order to avoid charging; however, this did not adversely affect the image quality. Figures 4-8 to 4-15 are examples of the SEM images that show the dispersion of the particles.

In general, the particles were not regularly dispersed. Flocculants of various sizes, several of which were very large, were found at the fracture sites. Figure 4-8 shows a low magnification (view field of 15.5 μm) for the *PMMA – Fe₃O₄* fracture surface. Several particles of different size are visible, appearing as small bright dots, relatively well dispersed along the image. Figure 4-9 shows another area of the

sample with the greater magnification (view field of $3.63\ \mu\text{m}$), and very few particles can be found having flocculated into two larger clusters. Figure 4-10 comes with a low magnification (view field of $12.8\ \mu\text{m}$) for the PS- Fe_3O_4 fracture surface demonstrating dispersed particles; the particles are lower in number than those of the PMMA- Fe_3O_4 surface.

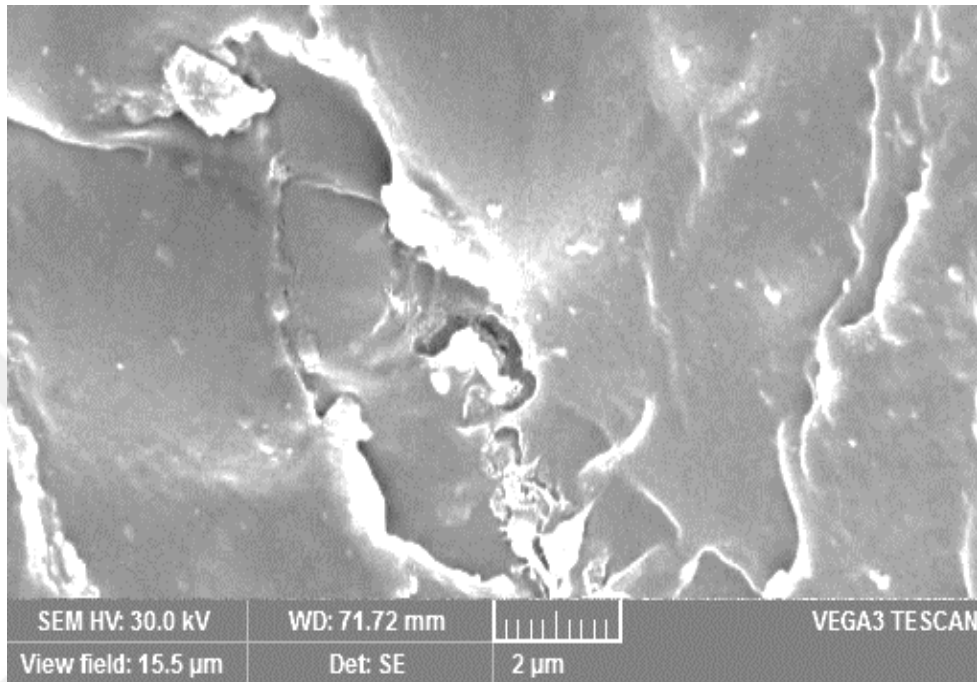


Figure 4-8 SEM image at low magnification view of particle dispersion for s of *PMMA – Fe_3O_4*

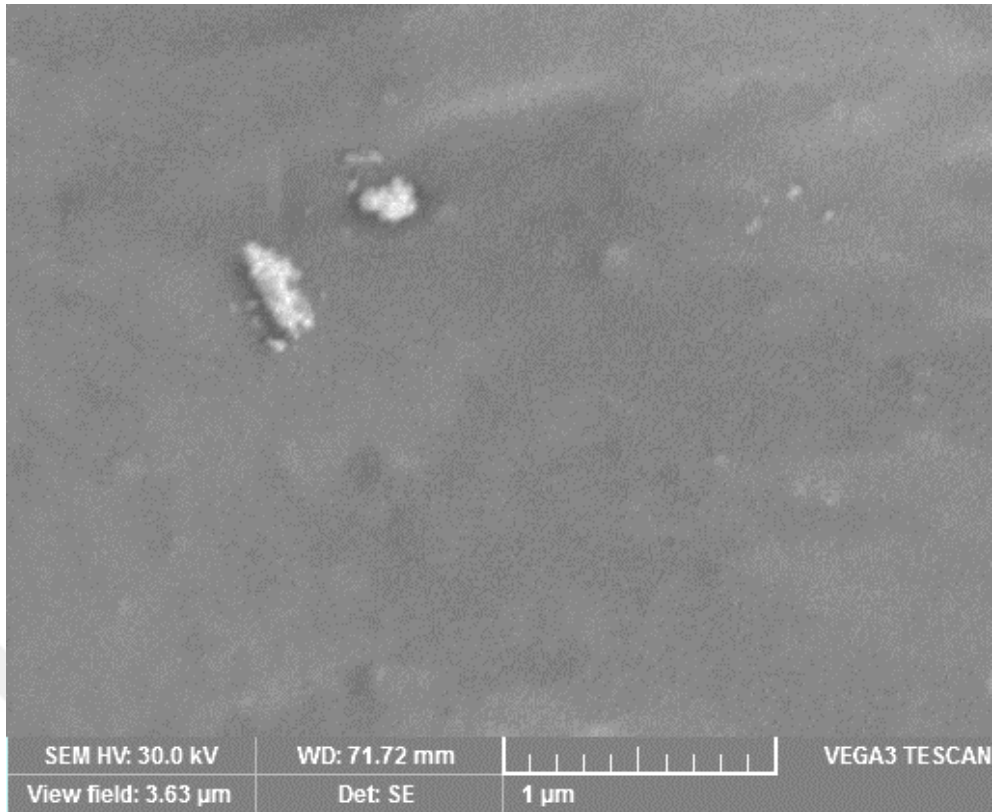


Figure 4-9 SEM image with close-up view of a small flocculant for s of *PMMA – Fe₃O₄*

With finer inspection of the particles at higher magnification (view field $1.44 \mu\text{m}$) shown in Figure 4-11, it can be seen that flocculation appears from the larger mass, appearing to be a variety of smaller particles giving their particular structure. It is not clear whether the particles flocculated just prior to or subsequent to the interaction with the polymer, so that the polymer layer at each smaller particle could be covered with an additional polymer coating or with a sputter coating. Figure 4-12 illustrates a very large flocculate within the fracture surface of the *PMMA – Al₂O₃* using low magnification (view field $11.6 \mu\text{m}$). At greater magnification shown in Figure 4-13, it is clear that these particles are mostly individual covered particles that have flocculated with each other.

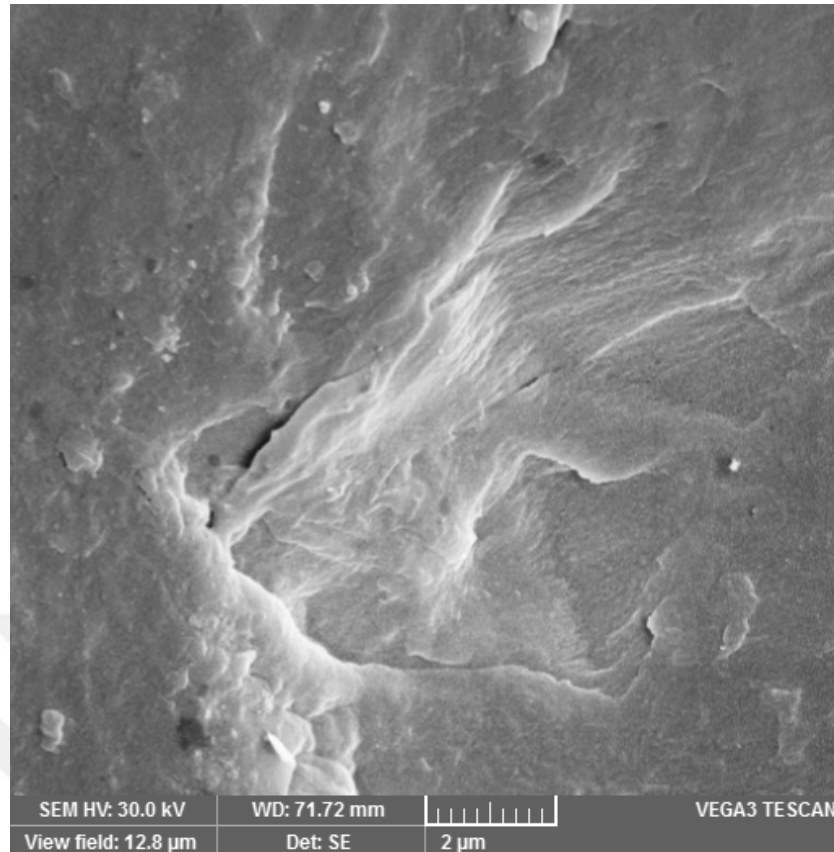


Figure 4-10 SEM image at low magnification view of particle dispersion for s of $PS - Fe_3O_4$

In the PMMA solution, it cannot be known whether the particles are flocculated once they are mixed and covered during the heating procedure of the tensile samples preparation. The tensile samples have a defined physical and thermal history. While the solvent is evaporating in the vacuum oven, the samples typically bubble on top of the mold surface at a higher temperature. After the solvent is removed, a higher temperature and physical compression are applied to the samples inside the dog bone mold. Considering that the matrix molecules themselves tend to be moving throughout the two of these heating processes, there is a high probability of movement of particles throughout the matrix and residing in the same area.

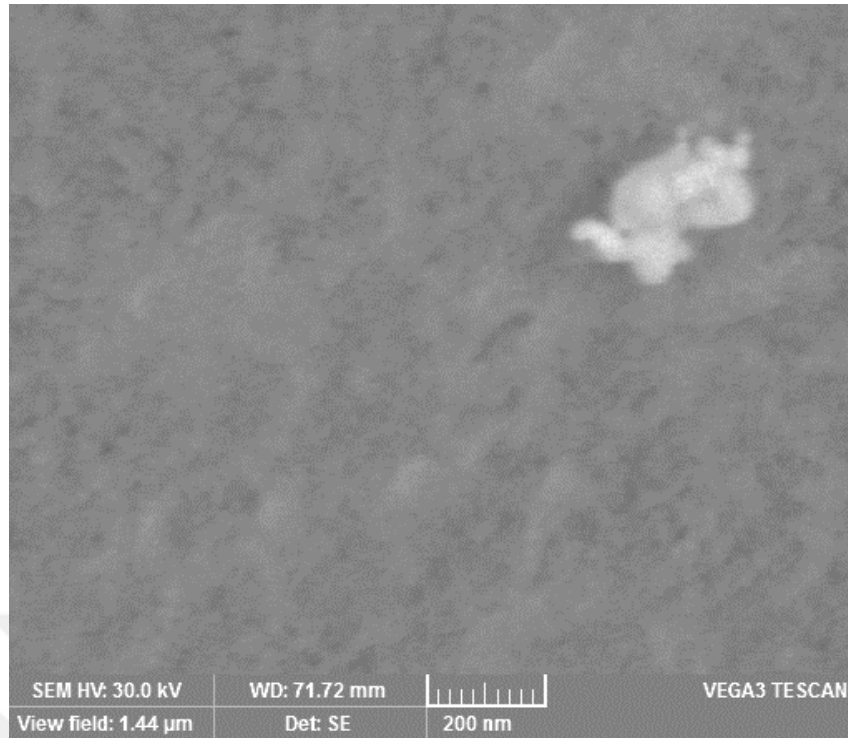


Figure 4-11 SEM image with close-up view of a small flocculant for s of $PS - Fe_3 O_4$

A very comparable mass of particles is obtained in the $PS - Al_2O_3$, as shown in Figure 4-14 at low magnification (view field $11.6 \mu m$). The larger magnification (view field $1.56 \mu m$) illustrates very specific separation among the particles at this mass, as shown in Figure 4-15. Every image reveals a certain amount of flocculation, but with size variation. In the $PS - Fe_3O_4$ system, the flocculant is approximately $200 \times 100 nm$ in size. In contrast, in the $PMMA - Al_2O_3$ and $PS - Al_2O_3$ systems, the flocculants are several microns in diameter. The SEM images indicate that the particles are not evenly dispersed throughout the dog bone samples and areas with no visible particles are found in each sample. A non-uniform dispersion could explain some of the ultimate strain and stress results.

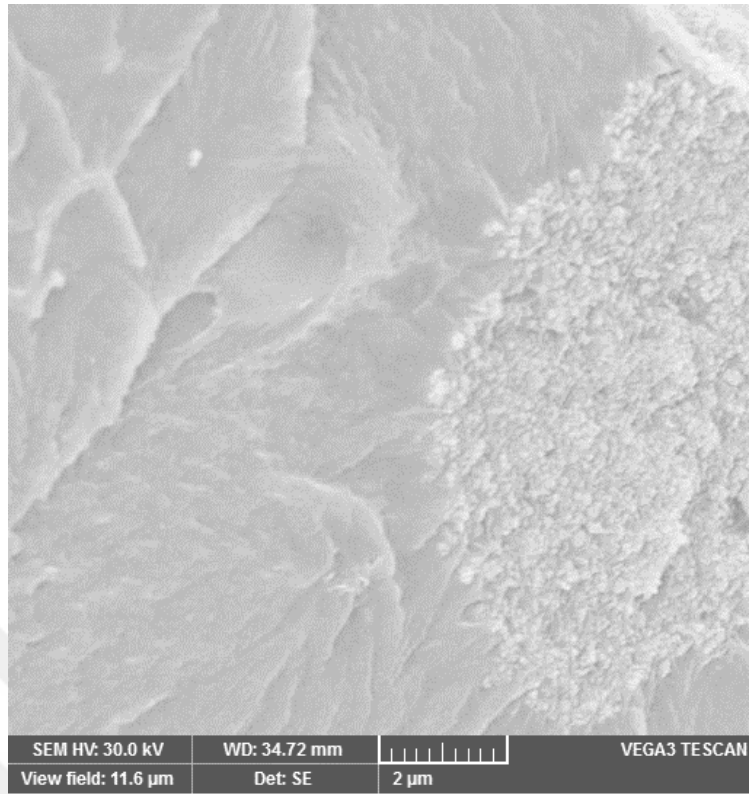


Figure 4-12 *PMMA – Al₂O₃* SEM image at low magnification view of a large flocculant

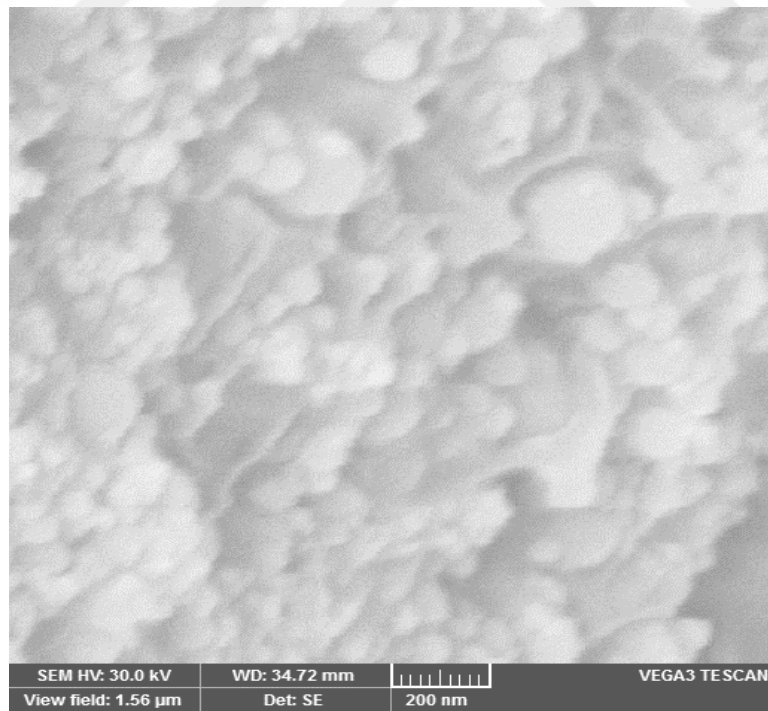


Figure 4-13 *PMMA – Al₂O₃* SEM image at close-up view of the particles within the flocculant

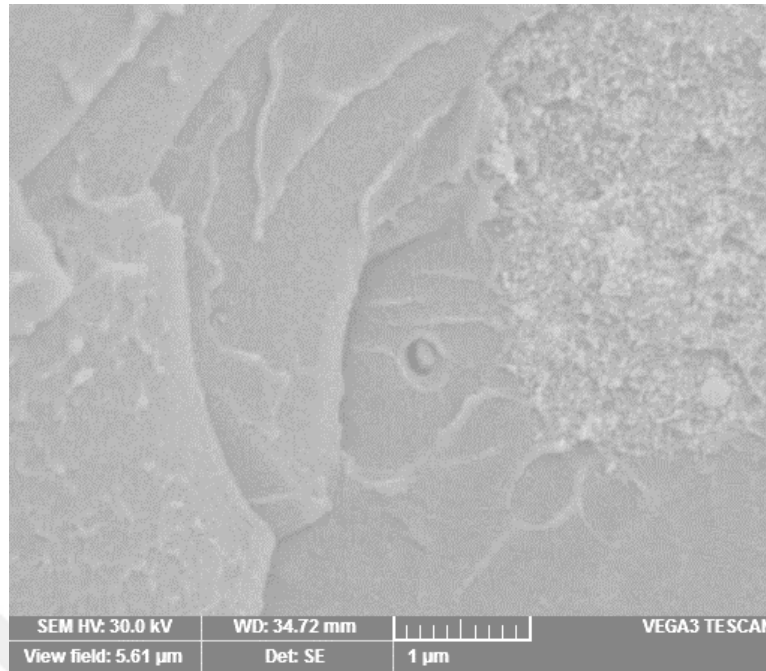


Figure 4-14 PS – Al₂O₃ SEM images at low magnification view of particle dispersion

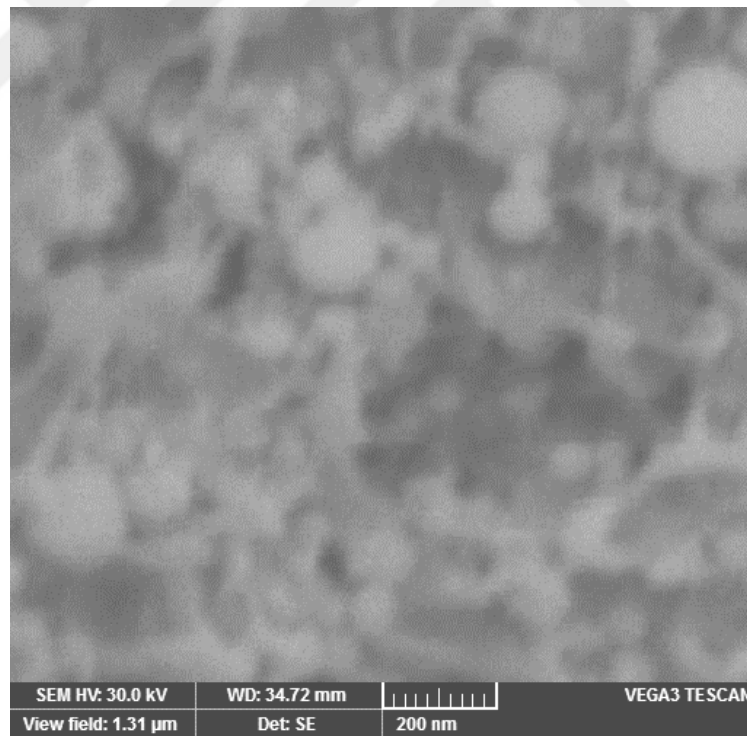


Figure 4-15 PS – Al₂O₃ SEM images with close-up view of a small flocculant

The complete particle size that has been measured in SEM images contains both the diameter of the metal oxide cluster and the thickness of the polymer layer bound to the surface of the cluster. As a result of determining the diameter of the metal oxide clusters based on reference data and presumed geometry, L_{eff} can be computed, as will be seen later in Section 4.6, which is a key part of the proposed approach characterization. Approximately 20 SEM images were inspected for every sample, and every observable particle was measured in each image, including the specific particles with flocculants that had been measured independently as they appeared to be capped with a polymer layer.

The SEM VEGA3 offered measuring tools were applied to measure particle sizes. Figures 4-16 to 4-19 show examples of the SEM images taken at the fracture location of the tested tensile specimen for the $PMMA - Al_2O_3$, $PMMA - Fe_3O_4$, $PS - Al_2O_3$ and $PS - Fe_3O_4$, respectively. It can be seen from those images that the particle diameter can be computed from the following equation:

$$d = \frac{2r}{Q_1} \times Q_{scale} \quad (4-1)$$

where, d is the particle diameter, r the particle radius in pixels, Q_1 the distance of scale measuring ruler in pixels and Q_{scale} the actual ruler scale. Applying Equation (4-1) in Figure 4-16, the diameter of the $PMMA - Al_2O_4$ is computed.

$$d = \frac{2 \times 44}{94} \times 200 \text{ nm} = 187.234 \text{ nm}$$

The same procedure is followed for every other image and 20 particles are selected for each tensile specimen. The average for all 20 measurements is computed, with results given in Table 4-4. The minimums, maximums and standard deviations for the 20 measured diameters are also listed in Table 4-4. For both polymer system groups, it is clear that the particles sizes of the Fe_3O_4 additive is generally larger than those of the Al_2O_3 additive with a similar polymer matrix. This difference is due to the initial particle sizes used in this work for Fe_3O_4 being 200 nm, whereas for Al_2O_3 it was 110 nm. It should be mentioned that the larger standard deviations mean there is a broad distribution of particle sizes for all the systems. For all the scanned images, there are some particles that are below the

initial diameter mentioned by the manufacturer. This means that either the procedure used in this work caused cluster separation or the manufactured particles had variations in their sizes that was not mentioned in the manufacturer's chemical specifications.



Figure 4-16 SEM image with measuring tools applied to the *PMMA – Al₂O₃* tensile test specimen at a fracture

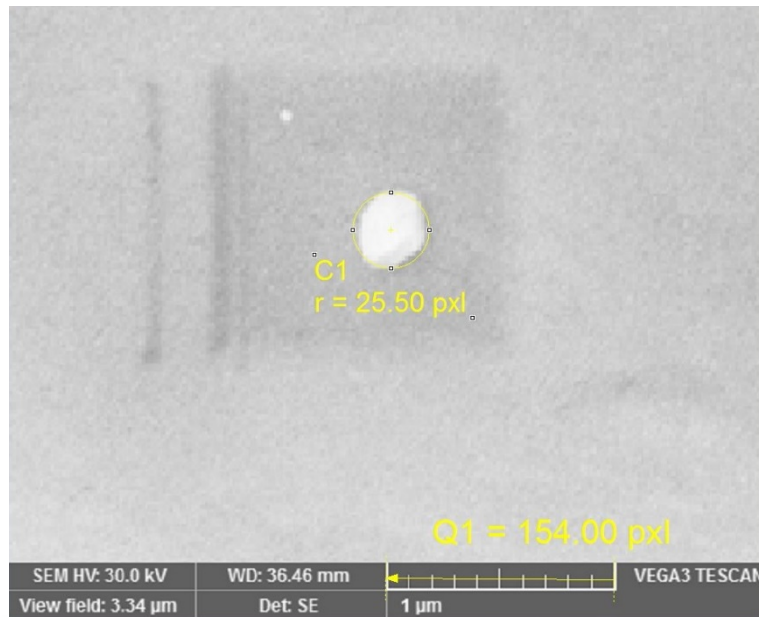


Figure 4-17 Image with measuring tools applied to the *PMMA – Fe₃O₄* tensile test specimen at a fracture

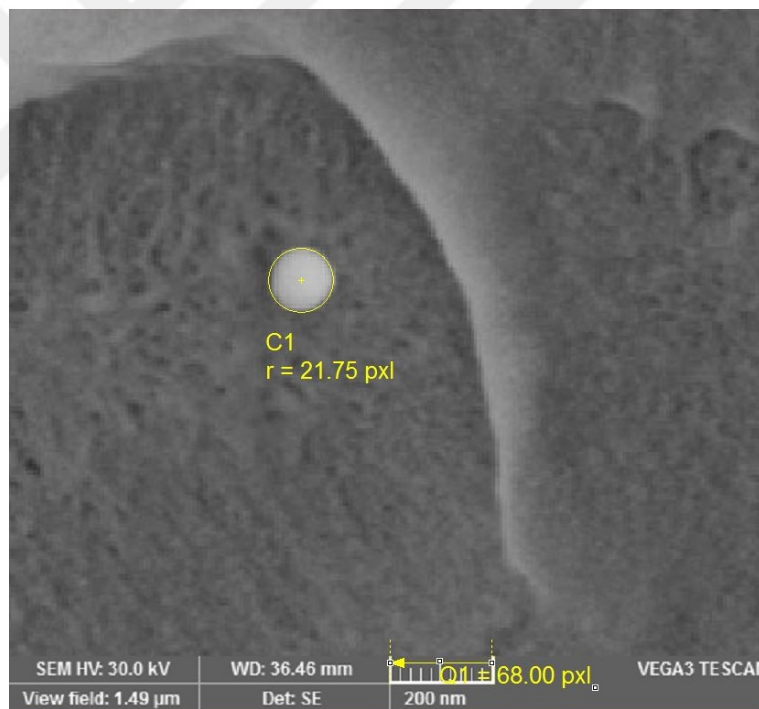


Figure 4-18 Image with measuring tools applied to the *PS – Al₂O₃* tensile test specimen at a fracture



Figure 4-19 SEM image with measuring tools applied to the $PS - Fe_3O_4$ tensile test specimen at a fracture

Table 4-4 Computed particles sizes in nm as measured from the SEM images

	$PMMA - Al_2O_3$	$PMMA - Fe_3O_4$	$PS - Al_2O_3$	$PS - Fe_3O_4$
Minimum measured diameter	138.0351	291.336	161.9022	290.47
Maximum measured diameter	245.3530	337.942	214.7137	374.28
Average diameter	201.117	375.628	184.6329	329.9
Standard deviation	32.4585	27.546	29.7534	25.573

4.4 Fourier Transform Infrared Spectroscopy (FTIR)

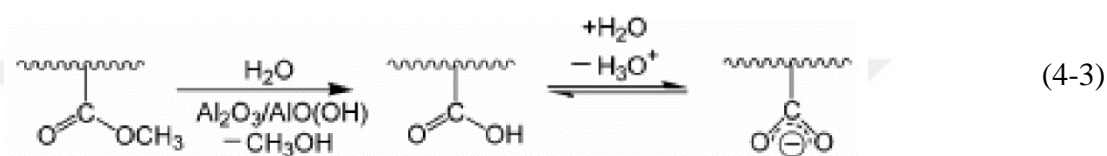
The FTIR is used to calculate the density of the interphase characterization by examining the bonding mechanism in the PMMA-based systems. The chemical description for the interaction of the PMMA and aluminum oxide surfaces is well

established. The bonding operation between the PMMA chain segments and the aluminum oxide nanoparticles surface is as follows:

Atmospheric water vapor reacts with the aluminum oxide nanoparticle surface molecules creating hydroxide surface groups [40]:



This hydration reaction can occur with various metal oxides, such as Al, Cr, Co, and Cu. The occurrence of the OH group in the nanoparticle surface helps hydrolysis for the PMMA ester group to create either a COOH acid group or its conjugate COO⁻ base group, in accordance with the following reaction.



The COO⁻ group immediately interacts with the positively charged Al atoms to build a bond between the polymer segment and the aluminum oxide nanoparticle surface. This bonded segment is an anchoring point for the PMMA chain.

A FTIR is applied to the PMMA-capped Fe_3O_4 and Al_2O_3 nanoparticles to ensure the interaction of the PMMA segments with the nanoparticles. The objective is to ensure that this bonding occurs as discussed earlier, and then to turn that bonding into an interphase structure. Other work has revealed that specific peaks with the IR spectrum demonstrate the presence of bonding between the PMMA and a metal oxide surface. Table 4-5 illustrates the peak ranges and specific bonds pointed by the peaks formerly identified [40].

Table 4-5 Infrared absorption bands of PMMA segment adsorption on Al_2O_3 surfaces

Peaks	Indicator	Peak assignment
2500-3200	Lower absorbance	O—CH ₃ bond is broken
1731	Lower absorbance	C=O is no longer isolated
1683	Peak height	COO ⁻ group concentration
1110-1210	Inverse peak ratios	C—C and C—O stretching modes

The FTIR spectra for the two PMMA systems are tested for these specific bands. Figures 4-20 to 4-23 show the focused part of the FTIR spectra for the PMMA-capped Al_2O_3 and Fe_3O_4 nanoparticles in a solution of chlorobenzene. By examining these spectra to find the PMMA adsorbed in the chlorobenzene, the bands showing the particle-polymer bonding tend to be effortlessly apparent. The Fe_3O_4 and Al_2O_3 spectra can be practically the same in absorbance across the entire spectrum.

Figure 4-20 implies the lower absorbance for the 2850 peak for the PMMA adsorbed on both the Al_2O_3 and Fe_3O_4 particles. The lower adsorbance denotes the initial step in reaction (4-3), the detachment from the methyl group. The lower adsorbance of the 1731 peak in comparison to the PMMA-chlorobenzene spectra in Figure 4-21 implies that some C=O bonds inside the ester groups could not be isolated; so they are hydrolyzed to create carboxylic acid (COOH) and carboxylic base (COO⁻) groups, the other steps of the reaction (4-3).

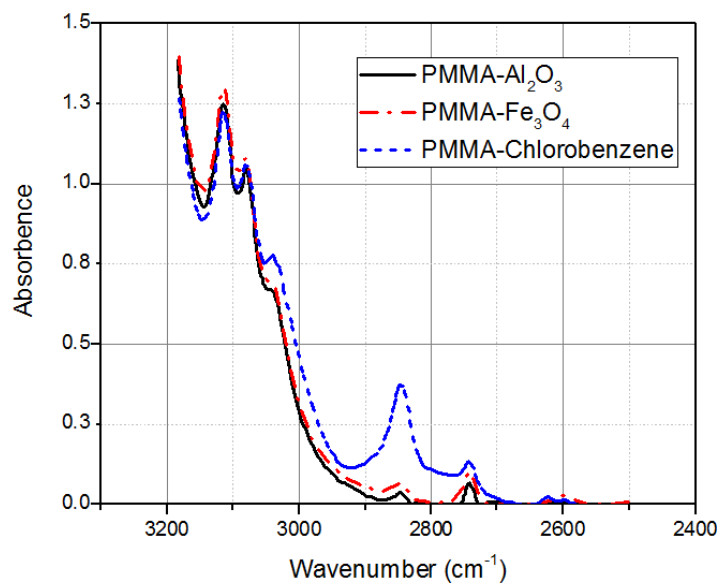


Figure 4-20 FTIR spectra for PMMA – Al₂O₃, PMMA – Fe₃O₄, and PMMA – chlorobenzene systems showing peak indicators for the 2843.8 band indicating broken O—CH₃

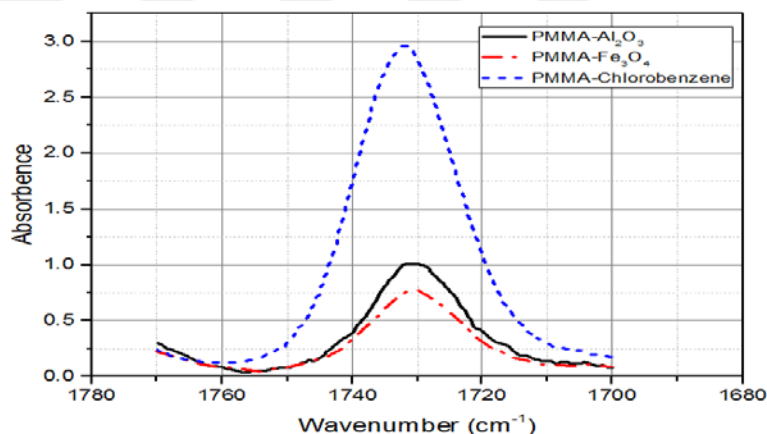


Figure 4-21 FTIR spectra for PMMA – Fe₃O₄, PMMA – Al₂O₃, a PMMA – chlorobenzene system showing the peak indicators for the 1731 band indicating C == O is no longer isolated in some PMMA segments

The presence of these peaks and signs ensures the forecasted bonding process involving PMMA and aluminum oxide. The similarity between the PMMA – Al₂O₃ and PMMA – Fe₃O₄ spectra implies the adhesion mechanism for the PMMA on the magnetite nanoparticles is similar.

Considering that the PMMA segment's carboxylic base (COO-) participates inside the bonding for the particle surface, quantifying the number of participating groups is able to assist an assessment of the number of bonds. The 1683 cm^{-1} absorption band, illustrated in Figure 4-22, corresponds to the asymmetric stretch of the COO- group, which is a sign of the COO- group bonding with the surface. Considering the ratio of the COO- groups taking part in bonding (1683 absorbance) with the ester groups which can no longer be isolated (1731 absorbance) describes the concentration of the COO- group. Using the peak height provided by the Origin Pro 2015 computer software, the height of the 1683 and 1731 peaks for the *PMMA – Al₂O₃* and *PMMA – Fe₃O₄* have been estimated with baselines identified using the software tool.

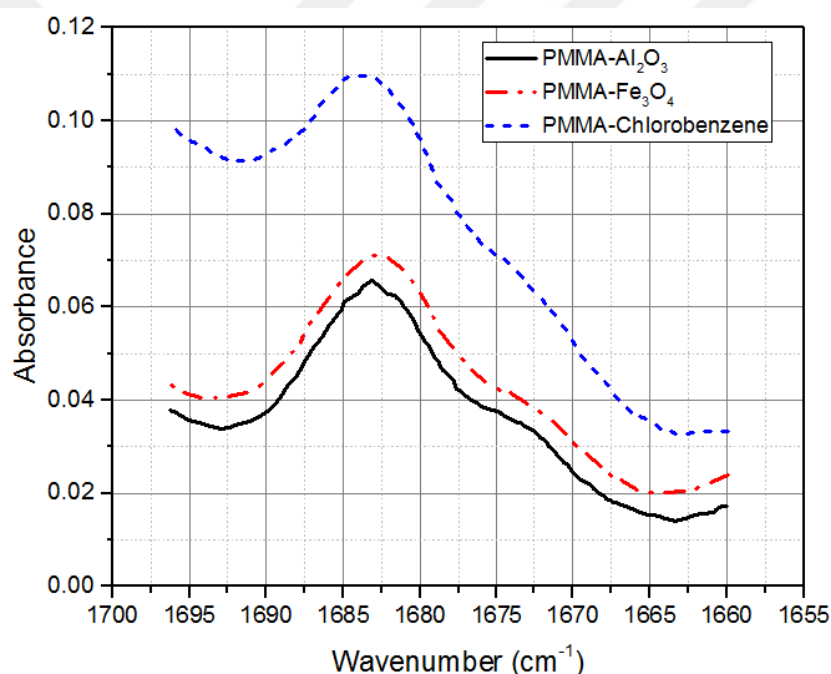


Figure 4-22 FTIR spectra for PMMA – Al₂O₃, PMMA – Fe₃O₄, and PMMA – chlorobenzene systems showing the 1683 cm^{-1} band indicating the absorbance of the carboxylic base (COO) groups

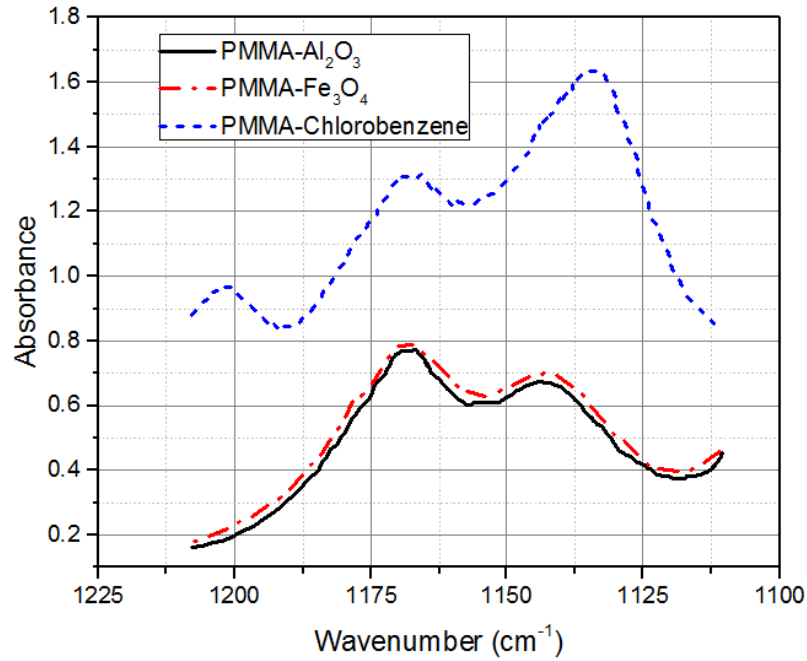


Figure 4-23 FTIR spectra for *PMMA – Al₂O₃*, *PMMA – Fe₃O₄*, and *PMMA – chlorobenzene* systems showing the 1166.7 and 1143 cm^{-1} bands. Note the shift in peak ratio between the chlorobenzene and nanocomposite spectra.

The PMMA's surface configuration change of a nanoparticle produces cooperative symmetric and antisymmetric extensions of the C—O and C—C groups. The relative intensity changes of the 1143 and 1166.7 infrared absorption bands represent these changes in the configuration. The change within the relative intensity is obvious when comparing the PMMA capped nanoparticle spectra with the PMMA-chlorobenzene spectrum, as seen in Figure 4-23. The segment portions of the polymer undergoing the changes in the configuration that represent the bonding can be indicated by the ratio of these two groups. The complete number of PMMA carboxylate groups which experience hydrolysis and become anchored on the surface can be computed through the ratio of the portions experiencing change in configuration as well as the concentration in the bonding group (COO). The number of anchoring points per chain can be computed by multiplying this number and the number of PMMA carboxylate groups by the average segment per polymer chain as given in Equation (4-4) [41].

$$Ac = \frac{E_{1683}}{E_{1731}} \cdot \frac{E_{1143}}{E_{1166.7}} \cdot \frac{N_{monomers}}{N_{chains}} \quad (4-4)$$

where, A_c is the number of anchor per chain, E_{1683} the absorbance intensity of the 1683 cm^{-1} infrared absorption band, E_{1731} the absorbance intensity of the 1731 cm^{-1} infrared absorption band, E_{1143} the absorbance intensity of the 1143 cm^{-1} infrared absorption band, $E_{1166.7}$ the absorbance intensity of the 1166.7 cm^{-1} infrared absorption band, $N_{monomers}$ the total number of carboxylate groups computed by Equation (4-6) and N_{chains} the total number of chains in the sample computed by Equation (4-5) [37].

$$N_{chains} = \frac{M_{sample} \cdot w_{polymer} \cdot N_A}{\bar{M}_w} \quad (4-5)$$

where M_{sample} is the sample mass in (g), $w_{polymer}$ the polymer mass fraction as estimated from the TGA data [%], N_A the number of chains per mole (Avogadro's Number) [chains/mole] and \bar{M}_w the weight average molecular weight of polymer [g/mole].

$$N_{monomer} = \frac{\bar{M}_w \cdot N_{chains}}{M_{w-monomer}} \quad (4-6)$$

where $M_{w-monomer}$ is the molecular weight of the monomer [g/mole].

The number of anchors per chain is computed using the FTIR spectra results and Equation (4-4) for the both the PMMA-based nanocomposites, which is given in Table 4-6.

The results in Table 4-6 differ from the given results of previous studies which used the same procedural approach. Tannenbaum, et al., [2] calculated that cobalt oxide nanoclusters formed in the presence of the PMMA ($\bar{M}_w = 330,000$) formed 855 anchoring points per chain. In this study, the number of anchors computed for several different molecular weights of the PMMA, demonstrates that with longer, more flexible chains, the effective penalty for the loss of configurational entropy is a result of chain confinement on the surface decreases. The robust interaction of the polymer along with the surface outweighs the entropic loss and the more flexible chains will form more anchoring points along the surface.

Table 4-6 Number of anchors per chain computed from FTIR results for $PMMA - Al_2O_3$ and $PMMA - Fe_3O_4$

	$PMMA - Al_2O_3$	$PMMA - Fe_3O_4$
E_{1683}	0.06512	0.07115
E_{1173}	1.00994	0.76689
E_{1143}	0.67341	0.69663
$E_{1166.7}$	0.76575	0.77404
N_{chains}	6.07E+14	1.23E+15
$N_{monomer}$	2.11E+18	4.22E+18
Ac	197.11	286.476

It is expected that the 400,000-molecular weight PMMA in this work will produce a higher number of anchoring points. In contrast, the results in this work are lower due to the difference in reactivity between the Al_2O_3 used in this work and the Co_2O_3 used in the study [2].

The forming clusters are capped by the PMMA chains which limit nanoparticle aggregation. In the reactive state of the nanoparticles during the decomposition process, polymer chains are produced. Those reactive sites may have increased the probability of the PMMA chains bonding to the surface. This work, additionally, applied pre-formed nanoparticle clusters that have been pre-processed and limited in particle size. The surfaces of these particles are generally much less reactive and give reduced energetic drive for bonding with the PMMA.

4.5 Thermal Gravimetric Analysis TGA

To estimate the weight fraction of the polymer layer adsorbed on the metal oxide particles, the TGA decomposition test is performed. The change from the starting weight to the final weight of the sample provides the weight of the polymer burned off through the experimentation. This weight fraction data enables the computation of the volume of the polymer around the particles. TGA tests are run at

the highest temperature of 600°C, effectively higher than the decomposition temperature of each PMMA and PS although below the decomposition temperatures of the metal oxides, ensuring that the polymer layer comprises the full weight difference.

Figure 4-24 shows the PMMA-based system tests results, from which the polymer layer produced 9.3% of the $PMMA - Al_2O_3$ particles and 14.95% of the $PMMA - Fe_3O_4$ particles. It could be noted that the Fe_3O_4 surfaces are more reactive with the $PMMA$ since more chains are anchored to the surface. Moreover, it can be noted that many more tightly bound chains might shield the surface from other chains, possibly producing a lower number but many more tightly bound chains [2]. Accordingly, that larger weight fraction of the bound chains on the Fe_3O_4 may occur as a result of weaker bonding of a large number of chains to the surface.

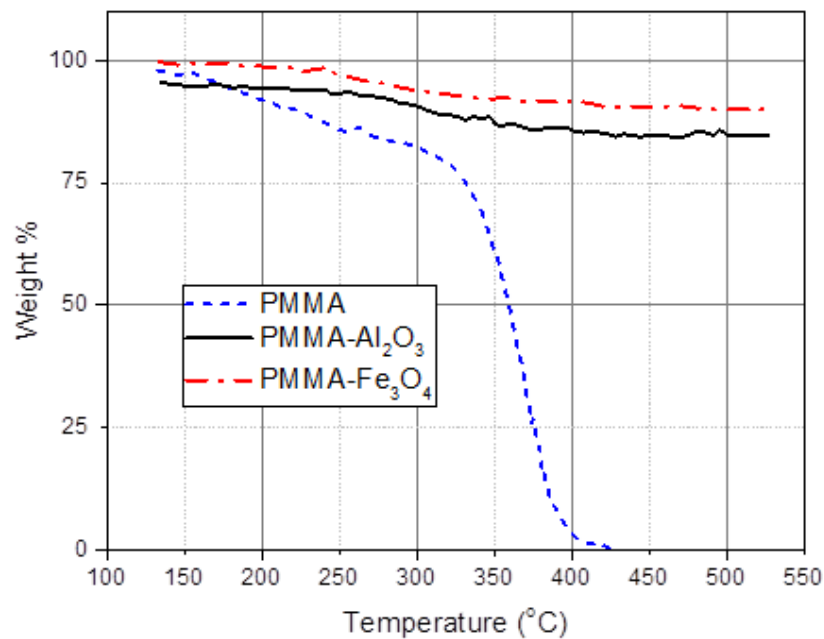


Figure 4-24 PMMA based system TGA results

Figure 4-25 shows the TGA results of the PS-based systems. It can be seen that it shows the same results. The polymer weight fraction for the $PS - Al_2O_3$ is found to be 9.7% and for the $PS - Fe_3O_4$ 12.1%. Provided there is less impression of configurational entropy loss as a result of high molecular chains, a similar polymer bonding holds for the PS-based systems. PS is mostly regarded as less reactive in

comparison to PMMA [2], although the data implies that it is more reactive with the Al_2O_3 surfaces compared to the Fe_3O_4 surfaces, forming a denser layer.

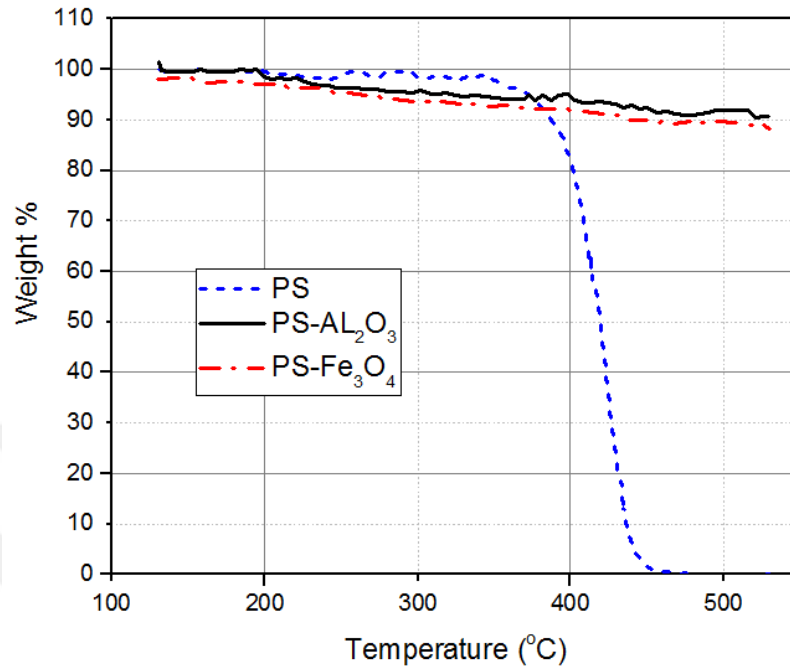


Figure 4-25 PS-based systems TGA results

4.6 Interphase Characterization

The number of anchoring points is computed using the total polymer mass directly adsorbed on the metal clusters from the TGA and the average size of the clusters from the SEM. From these data, the chains and the structure of the loops can be identified to determine the number of anchoring points. Figure 4-26a illustrates a schematic of the effective average polymer layer adsorbed on the nanoparticle and Figure 4-26b illustrates a schematic description of the actual number of free repeating units that exist in a polymer loop formed between the two anchoring points. It can be seen in Figure 4-26 that the interphase boundary extending from a particle surface can be identified from the thickness of the polymer layer directly adsorbed into the particle, L_{eff} . With the interphase region, the adsorbed polymer chains form loops and trains over the surface. Assuming that the arrangement of the polymer inside the loops can be that associated with a random coil, it is possible to

estimate the minimum number of segments obtained in a loop based on the number of segments in the length of the random coil. The number of segments in the loop with the molecular weight of the polymer estimates the number of anchoring points per chain. The results of the SEM and TGA are combined to assess the number of anchoring points [43].

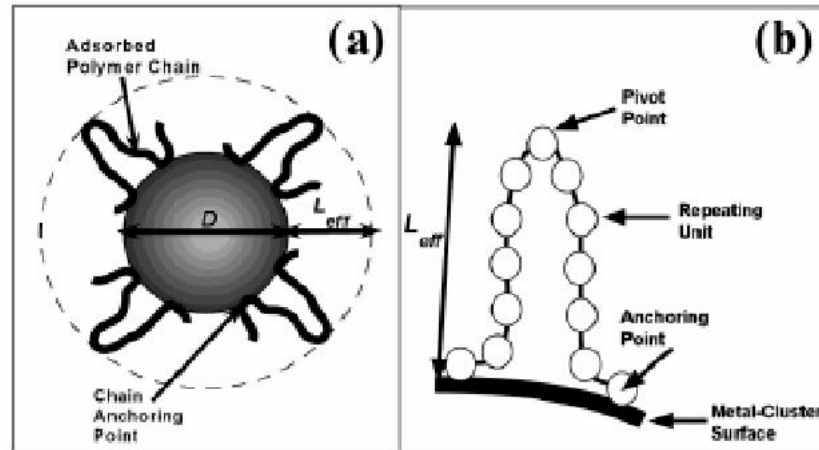


Figure 4-26 (a) The effective average polymer layer adsorbed on the nanoparticle (b) The actual number of free repeating units that exist in a polymer loop

By using both the weight fraction of the polymer in the capped-particle sample from the TGA and the average particle size from the SEM, the number of anchoring points per chain can be computed to obtain the formula of the thickness for the bound polymer layer around the particles. The thickness of the polymer layer, L_{eff} , is estimated by considering the total volume of a polymer-capped particle. The Total volume of the capped particle contains both the metal oxide cluster volume and the volume of the polymer layer bound to the surface.

$$V_{total} = V_{cluster} + V_{polymer} \quad (4-7)$$

The mass of the TGA sample, the weight fraction of the polymer and the number of clusters in the sample are used to compute the volume of the polymer adsorbed on the metal oxide cluster.

$$V_{polymer} = \frac{M_{sample} \cdot W_{polymer}}{N_{cluster} \cdot \rho} \quad (4-8)$$

where, M_{sample} is the sample mass (g) as given from the TGA results, $w_{polymer}$ the polymer mass fraction as obtained from the TGA data [%], $N_{cluster}$ the sample average number of clusters, and ρ the density of a thin polymer film [$\frac{g}{nm^3}$].

In this work, the density of the PMMA is evaluated at $1.21 g/cm^3$, or $1.21E - 21 g/nm^3$ and the density of the PS is evaluated at $1.032 g/cm^3$, or $1.032E - 21 g/nm^3$. The number of clusters in the sample is the proportion of the number of molecules in the sample and the number of molecules per cluster.

$$N_{clusters} = \frac{N_{molecules}}{N_{molecule/cluster}} = \frac{M_{sample} \cdot w_{cluster} \cdot N_A}{M_{w-molecule} \cdot \epsilon \left(\frac{D_{cluster}}{d_{molecule}} \right)^3} \quad (4-9)$$

where $N_{molecules}$ is the total number of molecules in the sample (eg Fe_3O_4 molecules), $N_{molecule/cluster}$ the number of molecules per cluster, $w_{cluster}$ the mass fraction of the polymer after decomposition of the polymer as obtained from the TGA results [%], N_A the number of chains per mole (Avogadro's Number) [chains/mole], $M_{w-molecule}$ the molecular weight of one metal oxide molecule in a cluster [g/mole], $D_{cluster}$ the average diameter of clusters [nm], $d_{molecule}$ the diameter of a molecule [nm], and ϵ the volume fraction of the molecules in the cluster, evaluated at 0.7.

The diameter of a molecule is computed based on the manufacture-provided density of each metal oxide molecule.

$$atoms / nm^3 = \frac{N_A \cdot \rho_{molecule}}{M_{w-molecule}} \quad (4-10)$$

where $\rho_{molecule}$ is the density of a molecule [g/nm^3].

Inverting Equation (4-7) provides the volume of a single atom.

$$nm^3 / atom = \frac{M_{w-molecule}}{N_A \cdot \rho_{molecule}} \quad (4-11)$$

The volume of a spherical atom can be expressed as $\frac{4\pi}{3} r^3$; solving for r to attain the diameter of the atom:

$$r = \left(\frac{3M_{w-molecule}}{4\pi \cdot N_A \cdot \rho_{molecule}} \right)^{\frac{1}{3}} \quad (4-12)$$

$$d_{molecule} = 2r \quad (4-13)$$

Using Equation (4-9), the diameter of a Fe_3O_4 molecule is 0.53 nm and an Al_2O_3 molecule is 0.43 nm. Assuming the clusters are geometrically spherical, the volume of a metal oxide cluster without an adsorbed polymer layer is

$$V_{cluster} = \left(\frac{4\pi}{3} \right) \left(\frac{D}{2} \right)^3 \quad (4-14)$$

where D_{av} is the average diameter of the clusters [nm]

The polymer capping layer adds a layer of thickness, L_{eff} , to each side of the diameter measurement, $D_{av} + 2L_{eff}$, so the total cluster volume with the adsorbed polymer layer is

$$V_{total} = \left(\frac{4\pi}{3} \right) \left(\frac{D_{av} + 2L_{eff}}{2} \right)^3 \quad (4-15)$$

With these two equations for V_{total} , an equation can be derived for L_{eff} . Equation (4-15) rearranged in terms of L_{eff} is:

$$L_{eff} = \left(\frac{3}{4\pi} V_{total} \right)^{\frac{1}{3}} - \frac{D_{av}}{2} \quad (4-16)$$

Substituting Equation (4-7) for V_{total} and simplifying the equation for L_{eff} by combining the TGA and SEM tests results:

$$L_{eff} = \left(\frac{3}{4\pi} (V_{cluster} + V_{polymer}) \right)^{\frac{1}{3}} - \frac{D_{av}}{2} \quad (4-17)$$

$$L_{eff} = \left(\frac{3}{4\pi} \left(\left(\frac{4\pi}{3} \right) \left(\frac{D_{av}}{2} \right)^3 + \frac{M_{sample} \cdot w_{polymer}}{N_{cluster} \cdot \rho} \right) \right)^{\frac{1}{3}} - \frac{D_{av}}{2} \quad (4-18)$$

$$L_{eff} = \left(\left(\left(\frac{D_{av}}{2} \right)^3 + \frac{3}{4\pi} \frac{M_{sample} \cdot w_{polymer}}{N_{cluster} \cdot \rho} \right) \right)^{\frac{1}{3}} - \frac{D_{av}}{2} \quad (4-19)$$

$$L_{eff} = \left(\left(\frac{D_{av}}{2} \right)^3 + \frac{3}{4\pi} \frac{w_{polymer} \cdot M_{w-molecule} \cdot \epsilon}{w_{cluster} \cdot N_A \cdot \rho} \left(\frac{D_{cluster}}{d_{molecule}} \right)^3 \right)^{\frac{1}{3}} - \frac{D_{av}}{2} \quad (4-20)$$

$$L_{eff} = \frac{1}{2} \left[D_{av}^3 + \frac{6}{\pi} \frac{w_{polymer} \cdot M_{w-molecule} \cdot \varepsilon}{w_{cluster} \cdot N_A \cdot \rho} \left(\frac{D_{cluster}}{d_{molecule}} \right)^3 \right]^{\frac{1}{3}} - \frac{D_{av}}{2} \quad (4-21)$$

The average number of repeating units, n_{eff} , in a particular average chain length is

$$n_{eff} = \frac{1 + \cos \theta}{2(1 - \cos \theta)} \left(\frac{L_{eff}}{\sigma_h \cdot l} \right)^2 \quad (4-22)$$

where θ is the rotation angle for the C-C bonds (110° for both PMMA and PS), σ_h is the steric hindrance factor (2.1 for PMMA and 2.3 for polystyrene at room temperature), and l is the C-C bond length of 1.56 Å.

The number of free repeating units that exist between two anchoring points, n_{loop} , is given by

$$n_{loop} = 2 \cdot n_{eff} - 1 \quad (4-23)$$

Within these equations, the number of anchoring points per chain can be computed:

$$Ac = \frac{N_{segments}}{n_{loop}} = \frac{\bar{M}_w}{M_{w-monomer} (2n_{eff} - 1)} \quad (4-24)$$

where $N_{segments}$ is the average number of segments in the chain, n_{loop} is the minimum number of segments present in a loop, \bar{M}_w is the average weight (molecular weight) of the polymer [g/mole], $M_{w-monomer}$ is the molecular weight of the monomer [g/mole] and n_{eff} is the number of segments in a random coil.

Using the data collected from the TGA and SEM and applying Equations (4-21 to 4-24), the number of anchoring points per chain is computed for all four nanocomposite systems, as shown in Table 4-7.

It can be seen from Table 4-7 that in the *PMMA – based* systems, *PMMA – Al₂O₃* produces a considerably denser interphase (15.880 anchors per chain) than *PMMA – Fe₃O₄* (1.005 anchors per chain). Similarly, for the *PS* based system, the *PS – Al₂O₃* produces a considerably denser interphase (16.363 anchors/chain) than *PS – Fe₃O₄* (2.553 anchors/chain), supporting the proposition that *Al₂O₃* is more reactive than *Fe₃O₄* with the polymer chains. The

PMMA – Fe_3O_4 creates a denser interphase than *PS* – Fe_3O_4 based on the relative reactivity of *PMMA* and *PS* [8], while the results of this work showed the opposite effect. The *PMMA* – Fe_3O_4 creates 1.005 anchors per chain, whereas *PS* – Fe_3O_4 creates 15.880 anchors per chain, indicating that *PS* is more reactive than *PMMA* with Fe_3O_4 . In addition, *PMMA* – Al_2O_3 creates 15.880 anchors per chain, whereas *PS* – Al_2O_3 creates 16.363 anchors per chain. Even if those results are not compatible based on relative reactivity assumptions, the difference in the results for the metal oxides across polymer systems is not significant.

Table 4-7 The computed interphase density results using the SEM and TGA data

	<i>PMMA</i> – Al_2O_3	<i>PMMA</i> – Fe_3O_4	<i>PS</i> – Al_2O_3	<i>PS</i> – Fe_3O_4
$D(nm)$	201.117	375.628	184.6329	329.9
$L_{eff}(nm)$	7.44	29.509	8.028	20.287
n_{eff}	126.439	1989.046	122.725	783.708
n_{loop}	251.878	3977.091	244.450	1566.4162
Ac	15.880	1.005	16.363	2.553

Many previous studies are following the same procedures stated in this work. Tannenbaum, et al., [2] computed that the number of anchors per chain of *PS* ($\bar{M}_w = 250,000$) on Co_2O_3 nanoclusters was 52.9. In this work, *PS* – Al_2O_3 ($\bar{M}_w = 400,000$) results in an estimated 16.363 anchors per chain; these results are in agreement. As stated previously, Tannenbaum, et al., computed that Co_2O_3 nanoclusters produced with the *PMMA* ($\bar{M}_w = 330,000$), created 855 anchoring points per chain; the same FTIR characterization procedure was taken. Table 4-7 shows that the 15.880 anchors per chain for the *PMMA* – Al_2O_3 is definitely different from the results of Tannenbaum, et al., which was 855 anchors per chain.

The large standard deviation in nanoparticle size injects uncertainty into the final results. The particle size is mostly a significant variable with this characterization approach and the large distribution of particle sizes shows that the

remarkably small deviation in values, as shown in Table 4-7, will mean that comprehensive analysis is not definitive. For instance, the particle size given in Table 4-7 for the $PMMA - Al_2O_3$ is 201.117, which has a standard variation of 32.4585. The maximum and minimum particle sizes obtained in the images, Table 4-4, were 138.0351 nm and 245.3530 nm, respectively.

A realization may be drawn when comparing the results for both systems, namely that $PMMA - Al_2O_3$ and $PMMA - Fe_3O_4$ with the two interphase characterization approaches produces results. As shown in Table 4-6, the FTIR approach estimates 197.11 and 286.476 anchors per chain for the $PMMA - Al_2O_3$ and $PMMA - Fe_3O_4$, respectively. In contrast, in Table 4-7, the TGA and SEM approach estimates 15.880 and 1.005 anchors per chain for the $PMMA - Al_2O_3$ and $PMMA - Fe_3O_4$, respectively. Although the results of both approaches are not compatible, it is helpful to use this TGA and SEM approach to check the results of the FTIR approach.

Provided the affordable nature of the particle sizes is required to synchronize the results, it could be expected that the particles shown by the SEM are smaller than the FTIR; in other words, the FTIR approach may be giving precise interphase density estimations. It should be kept in mind that the TGA and SEM strategy only measured the particles in the fracture surface, whereas the FTIR approach analyzed particles that could be located anywhere in the dog bone sample. It is possible that the large particles are on the fracture surface, whereas most of the particles inside the sample are smaller.

CHAPTER FIVE

CONCLUSIONS AND RECOMMENDATIONS

5.1 Conclusions

This work aims to study the effect of Al_2O_3 and Fe_3O_4 nanoparticle additives on the two-pure polymer system. The four systems produced $PMMA - Al_2O_3$, $PMMA - Fe_3O_4$, $PS - Al_2O_3$, and $PS - Fe_3O_4$ were tested. From the results of the present work, the following conclusions were/are drawn:

1. The Al_2O_3 nanoparticle additives with the two polymer systems, $PMMA - Al_2O_3$ and $PS - Al_2O_3$, produced improvements in the mechanical properties (ultimate tensile strength, % elongation (ϵ) and the ultimate strain (Δe_{ult}) when compared with the pure polymer PMMA and PS systems, whereas the other systems with Fe_3O_4 nanoparticle additives resulted in comparatively worse mechanical properties. Surprisingly, the addition of nanoparticles worsened the elastic modulus and perhaps yield strength of the systems in comparison to the pure polymer systems. Similar results were reported in [30].
2. SEM images showed that the Al_2O_3 and Fe_3O_4 nanoparticles in the two polymer nanocomposite systems were not regularly dispersed.
3. Interphase characterization revealed restricted interaction between the Al_2O_3 and Fe_3O_4 nanoparticles in both polymer matrices when compared with other research of similar systems. The lower number of anchoring points of the polymer chains on the metal oxide surfaces computed in this work results in a low-density interphase in all the nanocomposite systems. The low-density interphase across the high number of nanoparticles results in the loss of the elastic modulus.

4. The mixing procedure applied in this work to mix the pre-formed nanoparticles with a polymer solution was not useful for excellent dispersion or size distribution. The process does not gain from the polymer interaction with high-energy forming nanoparticles as has been reported in other studies. Critical flocculation was seen in the fracture sites of the dog bone samples, showing bad distribution.
5. FTIR analysis implies significant similarities between the interactions of Al_2O_3 and Fe_3O_4 nanoparticles with PMMA. The two interphase characterization approaches, nevertheless, did not provide consistent results. Factors contributing to the variance possibly involve large particle size distribution, flocculation, and lower nanoparticle reactivity.
6. A realization may be drawn when comparing the results for both systems (PMMA- Al_2O_3 and PMMA- Fe_3O_4) with the two-interphase characterization approaches used in this work such that the FTIR approach estimates 197.11 and 286.476 anchors per chain for PMMA- Al_2O_3 and PMMA- Fe_3O_4 , respectively. In contrast, the TGA and SEM approaches estimate 15.880 and 1.005 anchors per chain for PMMA- Al_2O_3 and PMMA- Fe_3O_4 , respectively. Although the results of both approaches are not compatible, it is helpful to use this TGA and SEM approach to check the results of the FTIR approach.
7. The particle size of the fractured nanocomposite surfaces shown by SEM is smaller than the FTIR. In other words, the FTIR approach may be providing precise interphase density estimations keeping in mind that the TGA and SEM strategy only measured the particles in the fracture surface, whereas the FTIR approach analyzed particles that could be located anywhere in the dog bone sample. It is possible that the large particles are on the fracture surface, whereas most of the particles inside the sample are smaller.

5.2 Suggestions for Future Works

The following are suggestions for future work:

- 1- Synthesize advanced polymer nanocomposite materials using different nanoparticles (e.g., TiN, SiC, WC, MgO).
- 2- Study the effect of nanoparticle additives (e.g., CeO, ZnO, Al₂O₃, WC, TiC, TiN, and SiC) on the microstructure and mechanical properties of polymer nanocomposite materials.
- 3- Study the effect of nanoparticle size and weight percentage on the mechanical properties of a polymer nanocomposite.
- 4- Study the wear characteristics of polymer based nanocomposite materials.
- 5- Fatigue characteristics evaluation of polymer based nanocomposite materials.
- 6- Evaluation of fracture toughness of nanocomposite materials using the Finite Element Method (FEM) and Design of Experiment (DOE) technique.
- 7- Study of the creep characteristics of polymer based nanocomposite materials.

REFERENCES

- [1] K. Rajkumar, P. Ranjan, P. Thavamani, P. Jeyanthi and P. Pazhanisamy, "Dispersion Studies Of Nanosilica In Nbr Based Polymer Nanocomposite," *Rasyan J. Chimestry*, vol. 6, no. 2, pp. 122-133 , 2013.
- [2] R. Tannenbaum, M. Zubris, K. David, K. Jacob, I. Jasiuk and N. Dan, "Characterization of Metal-Polymer Interfaces in Nanocomposites and the Implications to Mechanical Properties," *Physics and Chemistry*, vol. 110, no. 5, pp. 2227-2232, 2006.
- [3] J. Park and S. Jana, "The Relationship Between Nano- and Micro-Structures and Mechanical Properties in PMMA-Epoxy-Nanoclay Composites," *Polymer*, vol. 44, pp. 2091-2100, 2003.
- [4] E. Reynaud, T. Jouen, C. Gauthier, G. Vigier and J. Varlet, "Nanofillers in Polymeric Matrix: A Study on Silica Reinforced PA6," *Polymer*, vol. 42, pp. 8759-8768, 2001.
- [5] C. Wu, M. Zhang, M. Rong and K. Friedrich, "Tensile Performance Improvement of Low Nanoparticles Filled-Polypropylene Composites," *Composites Science and Technology*, vol. 62, pp. 1327-1340, 2002.
- [6] S. Shang, J. Williams and K.-J. Soderholm, "How the work of adhesion affects the mechanical properties of silica-filled polymer composites," *JOURNAL OF MATERIALS SCIENCE*, vol. 29, no. 9, p. 2406–2416, 1994.
- [7] J. Jordana, K. I. Jacobb, R. Tannenbaumc, M. A. Sharafb and I. Jasiukd, "Experimental trends in polymer nanocomposites—a review," *Materials Science and Engineering*, vol. A 393, pp. 1-11, 2005.
- [8] P. Vollenberg and D. Heikens, "Particle Size Dependence of the Young's Modulus of Filled Polymers: 1. Preliminary Experiments," *Polymer*, vol. 30, pp. 1656-1662, 1989.
- [9] C.-M. Chan, J. Wu, J.-X. Li and Y.-K. Cheung, "Polypropylene/Calcium

- Carbonate Nanocomposites," *Polymer*, vol. 43, pp. 2981-2992, 2002.
- [10] L. Zhu and K. Narh, "Numerical Simulation of the Tensile Modulus of Nanoclay Filled Polymer Composites," *Journal of Polymer Science: Part B: Polymer Physics*, vol. 42, pp. 2391-2406, 2004.
- [11] J. Jancar, A. Dibenedetto and A. Dianselmo, "Effect of Adhesion of the Fracture toughness of Calcium Carbonate-Filled Polypropylene," *Polymer Engineering and Science*, vol. 33, no. 9, pp. 559-563, 1993.
- [12] V. Kovacevic, S. Lucic and M. Leskovic, "Morphology and failure in nanocomposites. Part I: Structural and mechanical properties," *Journal of Adhesion Science and Technology*, vol. 16, no. 10, pp. 1343-1365, 2002.
- [13] M. Aubouy and E. Raphael, "Scaling Description of a Colloidal Particle Clothed with Polymers," *Macromolecules*, vol. 31, pp. 4357-4363, 1998.
- [14] Z. Petrovic, I. Javni, A. Wasson and G. Banhegyi, "Structure and Properties of Polyurethane-Silica Nanocomposites," *Journal of Applied Polymer Science*, vol. 76, pp. 133-151, 2000.
- [15] J. Kardos, "The Role of the Interface in Polymer Composites — Some Myths, Mechanisms, and Modifications," *Molecular Characterization of Composite Interfaces*, pp. 1-11, 1985.
- [16] M. Alexandre and P. Dubois, "Polymer-layered Silicate Nanocomposites: Preparation, Properties, and Uses of a New Class of Materials," *Material Science and Engineering*, vol. 28, pp. 1-63, 2008.
- [17] B. Ash, J. Stone, D. Rogers, L. Schadler, R. Siegel, B. Benicewicz and T. Apple, "Investigation into the Thermal and Mechanical Behavior of PMMA/Alumina Nanocomposites, in Filled and Nanocomposite Polymer Materials," *Materials Research Society: Boston, MA*, pp. KK2.10.1-10.6, 2001.
- [18] M. Rong, M. Zhang, S. Pan, B. Lehmann and K. Friedrich, "Analysis of the Interfacial Interactions in Polypropylene/Silica Nanocomposites," *Polymer International*, vol. 53, pp. 176-183, 2003.
- [19] K. David, N. Dan and R. Tannenbaum, "Competitive adsorption of polymers on metal nanoparticles," *Surface Science*, vol. 601, no. 8, pp. 1781-1788, 2002.

2007.

- [20] N. Dan, " N., Effect of Polymer Adsorption on the Surface Tension and Flocculation of Colloidal Particles in Incompatible Solvents," *Langmuir*, vol. 16, pp. 4045-4048, 2000.
- [21] S. King, K. Hyunh and R. Tannenbaum, "Kinetics of Nucleation, Growth, and Stabilization of Cobalt Oxide Nanoclusters," *The Journal of Physical Chemistry B*, vol. 107, no. 44, p. 12097–12104, 2003.
- [22] Y. Ou, F. Yang and Z.-Z. Yu, "A new conception on the toughness of nylon 6/silica nanocomposite prepared via in situ polymerization," *Journal of Polymer Science: Part B: Polymer Physics*, vol. 36, pp. 789-795, 1998.
- [23] F. Yang, Y. Ou and Z. Yu, "Polyamide 6/silica nanocomposites prepared by in situ polymerization," *Journal of Applied Polymer Science*, vol. 69, pp. 355-361, 1998.
- [24] C. Zeng and L. J. Lee, "Poly(methyl methacrylate) and Polystyrene/Clay Nanocomposites Prepared by in-Situ Polymerization," *Macromolecules*, vol. 34, pp. 4098-4103, 2001.
- [25] W. D. Callister, *Materials Science and Engineering An Introduction*, USA: John Wiley & Sons, Inc., 2007.
- [26] D. Campbell, R. Pethrick and J. White, *Polymer characterization: physical techniques*, Cheltenham: S. Thornes, 2000.
- [27] J. Goldstein, D. E. Newbury, P. Echlin and D. Joy, *Scanning Electron Microscopy and X-Ray Microanalysis*, New York: Plenum Press, 1992.
- [28] H. Szymanski, *IR: Theory and Practice of Infrared Spectroscopy*, New York: Plenum Press. 375, 1964.
- [29] X. Wang and C. Zhang, "Preparation and Properties of the Polystyrene/alumina Nanocomposites," *Advanced Materials Research* , Vols. 557-559 , pp. 519-522, 2012.
- [30] B. J. Ash, D. F. Rogers, C. J. Wiegand, L. S. Schadler, R. W. Siegel, B. C. Benicewicz and T. Apple, "Mechanical Properties of Al₂O₃/Polymethylmethacrylate Nanocomposites," *POLYMER COMPOSITES*, vol. 23, no. 6, pp. 1014-1025, 2002.

- [31] C.-H. Chen, Y.-Y. Sun and C.-H. Wu, "THE MECHANICAL PROPERTIES OF POLYSTYRENE/Al₂O₃ NANOCOMPOSITES," in 17th Annual International Conference on Composites or Nano Engineering, Hawaii, USA, 2009.
- [32] J. Shelley, P. Mather and K. DeVries, "Reinforcement and Environmental Degradation of Nylon-6/Clay Nanocomposites," *Polymer*, vol. 42, pp. 5849-5858, 2001.
- [33] P. Sikora, E. Horszczaruk, K. Cendrowski and E. Mijowska, "The Influence of Nano-Fe₃O₄ on the Microstructure and Mechanical Properties of Cementitious Composites," *Nanoscale Research Letters*, vol. 182, no. 11, pp. 1-9, 2016.
- [34] L. Li, H. Zhao, W. Wang and F. F. Nie, "Preparation and properties of Fe₃O₄/PMMA nanocomposite films," *Advanced Materials Research*, Vols. 79-82, pp. 505-508, 2009.
- [35] Z. Guo, X. Liang, T. Pereira, R. Scaffaro and H. T. Hahn, "CuO nanoparticle filled vinyl-ester resin nanocomposites: Fabrication, characterization and property analysis," *Composites Science and Technology*, vol. 67, p. 2036–2044, 2007.
- [36] S. Jain, H. Goossens, F. Picchioni, P. Magusin, B. Mezari and M. v. Duin, "Synthetic aspects and characterization of polypropylene–silica nanocomposites prepared via solid-state modification and sol–gel reactions," *Polymer*, vol. 46, p. 6666–6681, 2006.
- [37] M. R. Nabid, M. Golbabaee, A. B. Moghaddam, R. Dinarvand and R. Sedghi, "Polyaniline/TiO₂ Nanocomposite: Enzymatic Synthesis and Electrochemical Properties," *International Journal of Electrochemical Science*, vol. 3, pp. 1117 - 1126, 2008.
- [38] K. Y. Lau and M. A. M. Piah, "Polymer Nanocomposites in High Voltage Electrical Insulation Perspective: A Review," *Malaysian Polymer Journal*, vol. 6, no. 1, pp. 58-69, 2011 .
- [39] S. M. Momeni and M. Pakizeh, "Preparation, Characterization and Gas Permeation Study of PSF/MgO Nanocomposite Membrane," *Brazilian*

- Journal of Chemical Engineering , vol. 30, no. 3, pp. 589 - 597, 2013.
- [40] R. Tannenbaum, S. King, J. Lecy, M. Tirrell and L. Potts, "Infrared Study of the Kinetics and Mechanism of Adsorption of Acrylic Polymers on Alumina Surfaces," *Langmuir*, vol. 20, pp. 4507-4514, 2004.
- [41] B. c. Smith, *Fundamentals of Fourier Transform Infrared Spectroscopy*, London: CRS press, 1996.
- [42] Y. Brechet, J.-Y. Cavaille, C. E. Y., L. Chazeau, R. Dendievel, L. Flandin and C. Gauthier, "Polymer Based Nanocomposites: Effect of Filler-Filler and Filler-Matrix Interactions," *Advanced Engineering Materials*, vol. 3, no. 8, pp. 571-577, 2001.
- [43] D. L. Ciprari, "Mechanical Characterization of Polymer Nanocomposites and the Role of Interphase," 2004.
- [44] S. Su, D. D. Jiang and C. A. Wilkie, "Methacrylate modified clays and their polystyrene and poly(methyl methacrylate) nanocomposites," *polymer advance technology*, vol. 15, pp. 225-231, 2004.
- [45] K. Rajkumar, P. Ranjan, P. Thavamani, P. Jeyanthi and P. Pazhanisamy, "Dispersion Studies of Nanosilica in NBR Based Polymer Nanocomposite," *RASAYAB Journal of chemistry*, vol. 6, no. 2, pp. 122-133, 2013.